Towards precision measurements of the Hubble constant with the Canadian Hydrogen Intensity Mapping Experiment

by

Tristan Pinsonneault-Marotte

B.Sc. Honours Physics, McGill University, 2016

A THESIS SUBMITTED IN PARTIAL FULFILLMENT
OF THE REQUIREMENTS FOR THE DEGREE OF

Master of Science

in

THE FACULTY OF GRADUATE AND POSTDOCTORAL STUDIES
(Astronomy)

The University of British Columbia
(Vancouver)

April 2018

Committee Page

The following individuals certify that they have read, and recommend to the Faculty of Graduate and Postdoctoral Studies for acceptance, the thesis entitled **Towards precision measurements of the Hubble constant with the Canadian Hydrogen Intensity Mapping Experiment**, submitted by **Tristan Pinsonneault-Marotte** in partial fulfillment of the requirements for the degree of **Master of Science in Physics**.

- Gary Hinshaw, Physics and Astronomy (Supervisor)
- Kiyoshi Masui, Physics and Astronomy (Examining Committee Member)

Abstract

The Canadian Hydrogen Intensity Mapping Experiment (CHIME) is a transit interferometer located at the Dominion Radio Astrophysical Observatory in Penticton, BC. It is designed to map large-scale structure in the universe by observing 21 cm emission from the hyperfine transition of neutral hydrogen between redshifts 0.8 and 2.5. CHIME will perform the largest volume survey of the universe yet attempted and will characterize the BAO scale and expansion history of the universe with unprecedented precision in this redshift range. CHIME achieved first light in the fall of 2017 and instrument commissioning is underway. In this work I present sensitivity forecasts and derive constraints on cosmological parameters given CHIME's nominal survey. The broad redshift range of the observations will enable tight constraints to be placed on the Hubble constant H_0 , independent of CMB or local recession velocity measurements. Precision measurements of this epoch will shed new light on the tension between direct measurements of the Hubble constant vs. those inferred from high-redshift observations, notably the CMB anisotropy. CHIME measurements together with a prior on the baryon density from measurements of deuterium abundance are enough to place constraints on H_0 at the 0.5% level assuming a flat ΛCDM model, with uncertainty increasing to $\sim 1\%$ if curvature is allowed to vary, or up to $\sim 3\%$ for a dark energy equation of state with $w \neq -1$. Including priors from CMB measurements, in the scenario where the datasets are consistent, narrows these uncertainties further, most significantly in the model where w is a free parameter.

Lay Summary

The Canadian Hydrogen Intensity Mapping Experiment (CHIME) is a radio telescope located in Penticton, BC. It is designed to survey a large volume of the universe to map the distribution of matter at the largest scales, distances broad enough to encompass entire groups of galaxies. By tracking the evolution of these structures over a significant fraction of the lifetime of the universe, CHIME will measure the expansion of space. The rate of expansion today has been measured using two very different methods, and their results disagree. CHIME will make a novel, independent measurement of this same quantity, and inform whether the current tension can be attributed to errors in the measurements or if the cosmological model needs to be modified. I have produced forecasts for the precision that CHIME will be able to achieve. I find that expected measurement errors are small enough to allow CHIME to distinguish between the conflicting observations.

Preface

This thesis is original, unpublished work by the author, Tristan Pinsonneault-Marotte, conducted as part of the CHIME collaboration, under the supervision and guidance of Gary Hinshaw. Some elements of the analysis and hardware contributions presented here were based on existing work, as cited in the text. In particular, some of the code used for the analysis was branched off existing work from Richard Shaw, available at the `neutrino-forecast` repository on Github. The contributions I made to the FLA power control modules were building on an effort led by Kwinten van Gassen, a student researcher also part of the CHIME team at UBC.

Table of Contents

List of Tables

List of Figures

Acknowledgments

I want to thank the entire UBC CHIME team for their guidance and support. It has been a privilege to participate in the development of one of the most exciting experiments in cosmology today, especially surrounded by an enthusiastic group of intelligent people from whom I have learned a great deal. In particular, I'll thank Gary and Kiyo for their advice over the course of preparing this thesis, and my office mates Carolin, Deborah, Mateus, and Looney who have been companions and mentors in grad school.

Introduction

We live in an age of precision cosmology, wherein theories so broad in scope as to describe the evolution of spacetime itself over billions of years can rigourously be put to the test. The simplest and most successful description of the Universe so far, the "cosmological standard model", is known as ΛCDM (for the cosmological constant Λ, a static model of dark energy, and Cold Dark Matter that are its defining features). Although the fundamental assumptions of this model remain unchallenged by observation, the nature of its major constituents – dark energy and dark matter – are not understood. Particularly pressing is the case of dark energy, which is found to be at least very close to a cosmological constant. However, its observed energy density is separated by orders of magnitude from the vacuum energy one expects from quantum field theory, which itself has achieved great experimental confirmation in particle physics. Even more confounding would be to find that dark energy is not constant but evolves dynamically. Setting observational constraints on the dark energy is one of the main goals of the Canadian Hydrogen Intensity Mapping Experiment (CHIME), a radio interferometer that will perform the largest volume survey yet attempted of the large scale structure of matter in the universe by measuring 21 cm emission over redshifts $z = 0.8$ to 2.5 (800-400 MHz), at a time when the universe was transitioning into the current period of accelerated expansion driven by dark energy. CHIME is currently in the final stages of commissioning and achieved first light at the end of summer 2017.

The telescope is a compact transit interferometer composed of four cylindrical reflectors (see Figure 1) with dimensions 100×20 m, each instrumented with 256 dual-polarization antennae. The structure has no moving parts. Its cylindrical geometry only focuses incoming light in one direction (east-west), creating a field of view shaped like a narrow band spanning from one horizon to the other. This band scans the sky as it drifts overhead due to the rotation of the Earth, exposing the instrument to the entire northern sky every day.

The 2048 inputs are digitized and correlated in an "FX" scheme before being saved to disk. The analog signal is alias sampled and channelized into 1024 frequency bins between 400-800 MHz (the "F" part), after which every pair of inputs is multiplied and integrated ("X"), typically into a time bin of 10 s. The correlated inputs are referred to as visibilities, and the full set forms a 2048×2048 hermitian matrix, for every frequency, for every time frame. This produces a raw data rate of around 135 TB per day. Although some of this information is redundant (which may be useful for calibration purposes), the large data volume allows for much greater mapping speeds than can be achieved with single-dish or few-baseline telescopes. The interferometric phases can be adjusted in

Figure 1: The CHIME cylinders, Dominion Radio Astrophysical Observatory, Penticton, BC. (Photo taken by Andre Renard)

the analysis stage to resolve angular structure within the broad primary beam, up to the diffraction limit of the longest baseline, effectively pointing the telescope in any direction after the fact.

The large scale structure in the distribution of matter in the universe is dominated by dark matter, which is five times more abundant than the matter we can observe directly. Since the dark matter can only be detected via its gravitational effects, observations of other astronomical phenomena are used as tracers of its density. Previous surveys of large scale structure have used individual galaxies to map the underlying web of dark matter, but this is a slow process since spectra must be acquired on every one to determine the redshift. Additionally, the high angular resolution necessary to observe single galaxies is not a requirement for mapping the large scale structure, the features of which are at much greater angular scales. The signal CHIME aims to measure is 21 cm emission from neutral hydrogen as a tracer of matter density, at the comparatively low resolution afforded by radio observations. Thus CHIME will not resolve individual galaxies, but measure an aggregate of all the 21 cm radiation within its large field of view, a technique refferred to as intensity mapping. This allows for a very fast mapping speed, as the entire sky can be imaged every night, rather than having to point at individual locations. The effectiveness of neutral hydrogen as a tracer of large scale structure has recently been confirmed by correlating intensity mapping observations from the Green Bank Telescope with galaxy surveys over a patch of sky at redshift $z = 0.8$, as reported by Masui et al. [11]. The two techniques are found to agree, bolstering the case for intensity mapping as a new way forward in the field.

Intensity mapping produces a 3-d map of the density of neutral hydrogen, with the third dimension given by frequency, or redshift. As light travels to us from a distant source, the expansion of

the universe dilutes its energy, effectively stretching the wavelength as a Doppler shift. The amount by which the observed 21 cm emission has been redshifted is a measure of the time and distance to the source. CHIME's frequency band of 400-800 MHz corresponds to redshifts of 2.5-0.8 on the rest frequency of 1420 MHz. This spans a period between $\sim 2-6$ billion years after the Big Bang. Such a large survey volume, covering a significant fraction of the lifetime of the universe, will allow CHIME to track the evolution of the large scale structure at high signal to noise. Precise measurements of the expansion history at intermediate redshifts have the potential to shed light on dark energy and the accelerated expansion of the universe. The primary goal of the experiment is to set experimental constraints on the dark energy equation of state, but this is by no means the only cosmological question that can be investigated using the rich dataset. Of particular interest are the constraints these observations may place on the Hubble constant, given the apparent tension between measurements at high and low redshift. CHIME will also make observations outside of cosmology, notably for pulsar timing and Fast Radio Bursts.

In this work I will present forecasts for constraints on the Hubble constant H_0 based on CHIME sensitivity estimates. I will also describe work I performed over the course of the master's towards the commissioning of the instrument.

Forecasts for contraints on H_0 with CHIME

1 The Hubble constant

The Hubble constant, H_0, is a measurement of the expansion rate of the universe today. It is named after Edwin Hubble, who first observed that galaxies are systematically moving away from us at a velocity that is proportional to their distance, suggesting that the space between them is itself expanding, and kickstarting the field of observational cosmology. This was in 1929 [8], and since then cosmology has undergone rapid development, with significant discoveries in theory and observation building up our current understanding of the universe on the largest scales. Originating from a Big Bang singularity, the universe plausibly underwent a period of rapid inflation followed by a more gradual cooling leading up to the formation of the structures we observe today: stars, galaxies, and on. Spacetime has a globally non-euclidean geometry and evolves dynamically in interaction with the energy content of the universe, as described by general relativity. Observations have found precise agreement with the theory for a universe made up mostly of cold dark matter (CDM) and a cosmological-constant-like dark energy (Λ), with matter accounting for only $\sim 5\%$ of the energy density today. This model is referred to as ΛCDM. The "dark" constituents of the universe are so named because apart from their gravitational effects they have never been directly observed, and currently have no counterparts in the standard model of particle physics which has been successful in describing all other domains within the reach of observation (up to a handful of notable exceptions).

Even putting aside the puzzle surrounding the nature of the dominant constituents of the universe, increasingly precise observations have begun to at least suggest inconsistencies in the standard ΛCDM model. One of these tensions arises from disagreement between independent measurements of H_0. There have been two prominent approaches to measuring the Hubble constant. The first attempts to measure the expansion rate directly by observing a large number of nearby galaxies and fitting the relationship between their recession velocities and distances. They are carried away by the expansion of space according to Hubble's law: $v = H_0 d$. This method relies on supernovae as standard candles to estimate the distance to individual galaxies, calibrated using a series of increasingly remote sources for which the luminosity can be estimated, known as the "distance ladder". It

must also separate or suppress the component of the measured velocity that is due to local orbital motions of the galaxies, and not cosmological expansion. Recent results from Riess et al. [14] using this technique give $H_0 = 73.48 \pm 1.66$km/s/Mpc (the strange choice of units is adapted to the quantities found in Hubble's law).

A second approach is to infer the value of the Hubble constant from measurements of the cosmic microwave background (CMB), at the limit of the observable universe, its light having been produced only a few hundred thousand years after the Big bang. The patterns of anisotropy in the observed CMB encode information about the relative abundances of the different energy constituents of the universe and the initial conditions of fluctuations in their otherwise homogeneous distribution throughout space. Excellent agreement with the data is found for a minimal six parameter ΛCDM model assuming a globally flat geometry. The value of the Hubble constant inferred in this way is $H_0 = 69.7 \pm 2.4$ km/s/Mpc for WMAP [7], and $H_0 = 67.51 \pm 0.64$ km/s/Mpc for Planck [13]. Note that the difference between these two can be attributed to the Planck data extending to higher angular resolution. If H_0 is evaluated using only the low resolution data common to both experiments, they are in good agreement. So the high-resolution end of the Planck data pulls H_0 lower. The CMB value is in tension with the local distance ladder result quoted above – Riess et al. [14] note a difference of 3.7σ with the Planck result. However, the value of H_0 thus derived is largely degenerate with curvature if the latter is allowed to be non-zero, which is why priors from local distance ladder measurements are necessary to obtain constraints on the energy density in curvature. Together, these datasets are consistent with a flat universe, with $\Omega_k = 0.04 \pm 0.040$ [13]. Allowing dark energy to deviate from the cosmological constant form also has the potential to alter the expansion history and modify the inferred value of H_0. So the apparent tension between CMB-only and local measurements of H_0 is encountered for a minimal model of the universe – flat with a cosmological constant – and adding additional freedom by allowing for non-negligible curvature or evolving dark energy may eventually be necessary. Alternatively, systematic errors in either measurement could be responsible for the disagreement. In either case, to make further progress precision measurements at an epoch much more recent than the CMB, when curvature and dark energy are both potentially important, will be useful in resolving the question.

Surveys of large scale structure at high-redshift searching for the imprint of baryonic acoustic oscillations (BAO, described in the following section) are a promising way forward. The BAO signature is present at all epochs since last scattering, opening the door to observations at periods between the production of the CMB and today, spanning essentially the full age of the universe. Already, the BAO signal has been detected by galaxy surveys at low redshifts ($z \lesssim 1$) – most notably by the Sloan Digital Sky Survey [2] – and this data has been used to tighten constraints on cosmological parameters from the CMB. See Addison et al. [1] for a thorough review of these efforts. The lack of spectral lines and slow mapping speeds prevent galaxy surveys from pushing to further redshift, but novel experiments like CHIME are aiming to sidestep this limitation with the use of hydrogen intensity mapping. CHIME will be sensitive to a redshift range of $0.8 - 2.5$, corresponding to a period $\sim 2 - 6$ billion years after the Big Bang. This is when the ΛCDM universe is expected to be

on the verge of transitioning from an energy distribution dominated by matter to one dominated by dark energy. If curvature is non-zero, this may also be a window in time when it could have briefly made a significant and detectable contribution to the energy density.

2 Measuring H_0 with BAO

2.1 Baryonic acoustic oscillations

Extrapolating the presently observed expansion of the universe back in time suggests it was once in a hot and dense state. At some point, the temperature of radiation would have been sufficient to ionize hydrogen, coupling photons and matter through Compton scattering. This represents a boundary beyond which the universe becomes opaque to the propagation of light. The discovery and subsequent observations of the cosmic microwave background (CMB) have confirmed this picture and characterized it to exquisite precision. The CMB is an image of the universe at this instant when it cooled sufficiently to allow hydrogen to form again and photons to travel unimpeded and reach us today. Although the temperature of the CMB is remarkably uniform over the entire sky (to a part in 10^4), the small anisotropies that are observed encode a wealth of information about the early universe.

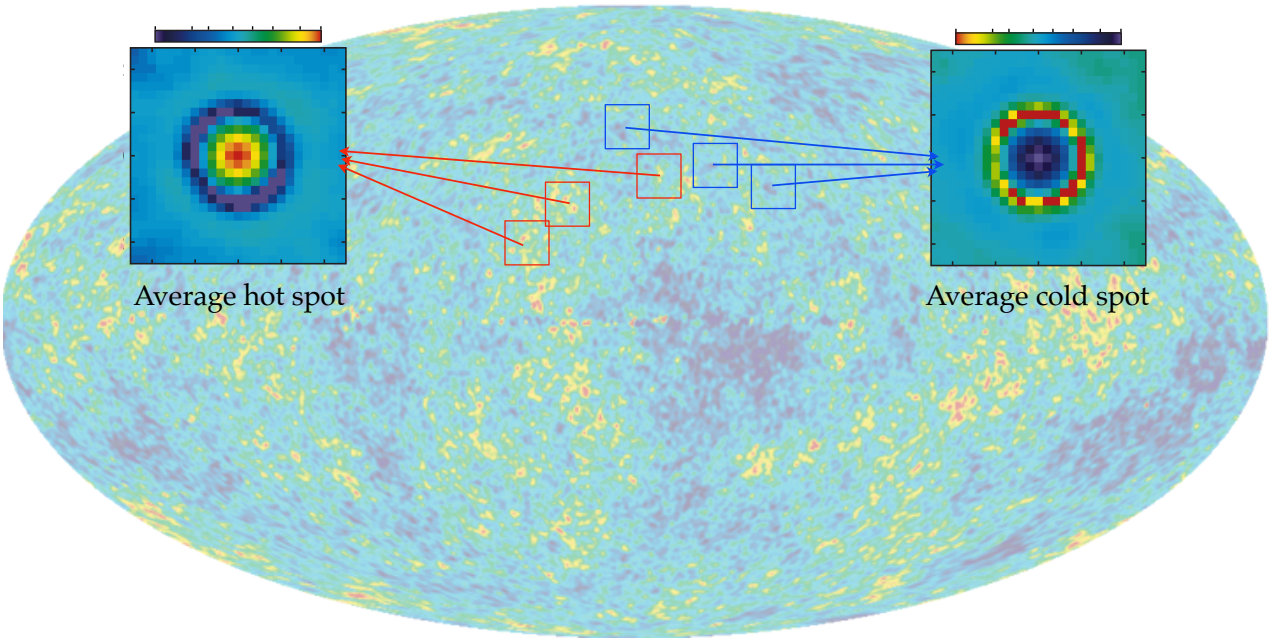

Figure 2: Stacks of hot and cold spots in the WMAP CMB anisotropy map. The BAO feature as an acoustic ring located at the sound horizon r_s. (Figure credit: Gary Hinshaw)

Temperature fluctuations are related to fluctuations in the matter density through the tight photon-baryon coupling (where baryon is taken to mean all non-dark matter, as is conventional). In this

regime, the photon-baryon plasma can support density waves (sound waves), with the restoring force provided by radiation pressure. These are the baryonic acoustic oscillations (BAO). Initial fluctuations in the matter density produce impulses that then propagate away at the sound speed of the plasma, c_s. When radiation decouples from matter, the restoring force vanishes and the wave-front gradually comes to a halt. The distance the wave travelled in the time before this decoupling is the sound horizon at recombination

$$r_s = \int_0^{t_*} \mathrm{d}t \frac{c_s}{a(t)} = \int_{z_*}^{\infty} \mathrm{d}z \frac{c_s}{H(z)} \,, \tag{1}$$

where the factors $a(t)$ and $H(z)$ account for the expansion over this period, as detailed in the following section. This scale is detected statistically in the anisotropies of the CMB, as illustrated in Figure 2. It is also present in the matter density fluctuations that eventually grew into the large scale structure of the late-stage universe. The characteristic scale of this feature is the same as given in Equation 1, apart from a relatively small correction to the bounds of the integral to account for the inertia of the density front that cause it to travel further after radiation decouples and the CMB is produced. This residual velocity is wiped out by gravitational drag, so the corrected scale is often referred to as the sound horizon at the end of the drag epoch. In what follows, I will use r_s and "sound horizon" to refer to the latter quantity.

2.2 Imprint of the BAO

The BAO left an imprint in the density field of matter at a characteristic scale corresponding to the radius they travelled before being frozen in place – the sound horizon at last scattering, r_s. As the universe continues to cool, the initial matter over and under-densities grow due to gravitational collapse to form stars, galaxies, and clusters – altering the initial distribution at increasingly large scales over time. The BAO scale is a sufficiently large distance to have survived as a coherent feature up to this point in cosmic history, largely unaffected by local growth of structure. The passive evolution of the BAO make it an ideal "standard ruler" to track the global expansion of space over cosmological timescales.

The BAO standard ruler is present along all three spatial dimensions, with no preference given to any choice of coordinates, but observationally, it can be detected in two orthogonal directions: in the angular distribution of matter on the celestial sphere (i.e. a spherical slice with the Earth at the centre), or radially, as density fluctuations along the line of sight, at depths determined by the redshifts of the measured signal. These directions will be referred to as perpendicular and parallel to the line of sight. They constrain two physical parameters of the cosmological model[1] independently.

The first is angular diameter distance, D_A, defined as the distance separating an observer from an object of known diameter l that they would infer given its apparent angular size $\Delta\theta$. In euclidean

[1]The overview of fundamental cosmological concepts that will follow is based on similar discussions found in the textbooks by Dodelson [5] and Weinberg [21].

space, the small angle approximation takes the familiar form

$$\Delta\theta = \frac{l}{D_A} \,. \tag{2}$$

In an expanding or curved space, this distance is in general different, since the trajectory of light travelling from the object is not a straight line. The specific geometry of the space is described by a metric, a prescription for measuring distances given some choice of coordinate basis, expressed as a set of coefficients $g_{\mu\nu}$: $\mathrm{d}s^2 = g_{\mu\nu}\,\mathrm{d}x^\mu\,\mathrm{d}x^\nu$. A foundational principle in cosmology is the assumption of homogeneity and isotropy – that there are no preferred locations or directions in the universe. This requirement greatly reduces the number of allowed metrics to describe spacetime, the most general expression being the Friedmann-Robertson-Walker (FRW) metric

$$\mathrm{d}s^2 = -\,\mathrm{d}t^2 + a^2(t)\left[\frac{\mathrm{d}r^2}{1-Kr^2} + r^2\,\mathrm{d}\Omega^2\right] , \tag{3}$$

where $a(t)$ is a scale factor, parametrizing the expansion of space over time, and K is the curvature, which can be negative, zero, or positive. For the special case of a static ($a \equiv 1$) and flat ($K \equiv 0$) space, this expression reduces to the Minkowski metric. It is a convention to define the scale factor today to be unity

$$a(t = t_0) \equiv 1 \,, \tag{4}$$

in which case $K > 0$ can be interpreted as the radius of curvature of the universe today.

In *coordinate* space, (t, r, θ, ϕ), light travels in straight lines, so it is straightforward to write down the angular diameter in the small angle approximation

$$\Delta\theta = \frac{l/a(t)}{r} \,, \tag{5}$$

where the physical extent l has been expressed in coordinate space by removing the effect of the scale factor $a(t)$ at the time light left the object, and r is the coordinate distance to the observer. This defines angular diameter distance (for an object of known physical diameter) as

$$D_A = \frac{l}{\Delta\theta} = a(t)r \,. \tag{6}$$

Information about the expansion history of the universe is thus encoded in D_A, through its dependence on the scale factor.

Coordinate distance r may not appear to be a physically meaningful quantity, but it is simply related to another useful distance measure in cosmology: comoving distance D_c. This is defined as

the distance travelled by light in time t with the effect of the scale factor removed

$$D_c(t) = \int_0^t \frac{dt'}{a(t')} = \int_0^r \frac{dr}{\sqrt{1-Kr^2}} = \begin{cases} \arcsin(r), & K > 0 \\ r, & K = 0 \\ \text{arcsinh}(r), & K < 0 \end{cases} \tag{7}$$

using the fact that the spacetime interval for light vanishes to turn the time integral into an integral over distance. So in flat space we have

$$D_A = D_c a(t) = \frac{D_c}{1+z} \,, \tag{8}$$

where I've taken the opportunity to define the redshift as $1+z = a^{-1}$.

So far, I've defined distances in a geometrical setting, but haven't considered how they change with the evolving universe. The dynamics of the standard cosmological model, in particular the history of $a(t)$, are dictated by the Einstein equations of general relativity, which take a simplified form for the FRW metric. One of them relates the evolution of the scale factor to the (uniform) energy density ρ

$$\dot{a}^2 + K = \frac{8\pi G \rho a^2}{3} \,. \tag{9}$$

This equation defines a critical density for which the curvature vanishes today

$$K = 0\Big|_{t=t_0} \Leftrightarrow \rho_{cr} = \frac{3(\dot{a}/a)^2}{8\pi G}\bigg|_{t=t_0} = \frac{3H_0^2}{8\pi G} \,, \tag{10}$$

where H_0 is the Hubble parameter, $H = \dot{a}/a$, evaluated today, at $t = t_0$. Using this definition, separate the different contributions to the energy density in terms of their ratio to the critical density today

$$\rho = \rho_{cr}(\Omega_\Lambda + \Omega_m a^{-3} + \Omega_r a^{-4}) \;;\; \Omega_i = \frac{\rho_i}{\rho_{cr}}\bigg|_{t=t_0} \,. \tag{11}$$

Ω_Λ is the energy density of the cosmological constant Λ which by definition doesn't evolve over time, Ω_m is the density of matter, diluting as a^{-3}, and Ω_r is radiation, evolving like a^{-4}. One way to understand the power of -4 diluting the radiation density is to think of photons with number density decreasing as a^{-3}, but also redshifting as their wavelength is stretched by the expansion of space, thus reducing their energy by an additional factor of a.

With these definitions, Equation 9 becomes

$$\left(\frac{H}{H_0}\right)^2 = \Omega_\Lambda + \Omega_m a^{-3} + \Omega_r a^{-4} - \frac{K}{H_0^2} a^{-2} \,, \tag{12}$$

evaluated at $t = t_0$,

$$1 = \Omega_\Lambda + \Omega_m + \Omega_r - \frac{K}{H_0^2} \,, \tag{13}$$

The deviation from flatness can be interpreted as an energy density in curvature

$$\Omega_k = -\frac{K}{H_0^2} = 1 - (\Omega_\Lambda + \Omega_m + \Omega_r) \,, \tag{14}$$

which leaves a final expression for the Friedmann equation governing the evolution of the scale factor with time

$$\left(\frac{H}{H_0}\right)^2 = \Omega_\Lambda + \Omega_k a^{-2} + \Omega_m a^{-3} + \Omega_r a^{-4} \,. \tag{15}$$

As a differential form, this equation is

$$\begin{aligned} \mathrm{d}t &= \frac{\mathrm{d}a}{aH_0\sqrt{\Omega_\Lambda + \Omega_k a^{-2} + \Omega_m a^{-3} + \Omega_r a^{-4}}} \\ &= \frac{-a\,\mathrm{d}z}{H_0\sqrt{\Omega_\Lambda + \Omega_k (1+z)^2 + \Omega_m (1+z)^3 + \Omega_r (1+z)^4}} \,. \end{aligned} \tag{16}$$

With this form, the integral for the comoving distance to a given redshift can be evaluated, such that the angular diameter distance is

$$D_A = \frac{1}{H_0(1+z)} \int_0^z \frac{\mathrm{d}z'}{\sqrt{\Omega_\Lambda + \Omega_k (1+z')^2 + \Omega_m (1+z')^3 + \Omega_r (1+z')^4}} \,. \tag{17}$$

This expression depends on the parameters of the cosmological model H_0 and $\{\Omega_i\}$. Observational constraints on these can therefore be obtained from measurements of the apparent angular diameter $\Delta\theta$ and redshift of an object of known size, the BAO feature in this case.

The scale of the BAO tracks the expansion of space, so its physical size is changing over time, going like $a(t)r_s$, where r_s is it size in comoving coordinates (measured today, at $a = 1$). The sound horizon is not measured by surveys of large scale structure such as CHIME, it must be taken as an additional parameter or prior information. So the angular measurement on its own is a combined measurement of D_A and r_s, for a given redshift

$$\frac{D_A(z)}{r_s} = \frac{1}{(1+z)\Delta\theta(z)} \,. \tag{18}$$

Equations 17 and 18 are the model and data for measurements of the BAO scale in the transverse direction.

In the direction parallel to the line of sight, the coordinate axis of the observations is redshift (or frequency), so physical distances must be mapped into separations in redshift. Imagine two photons emitted a different distance from the observer along the line of sight at times t_1 and t_2 such that they arrive simultaneously. One will have travelled further than the other by the time it is detected, so it will have been redshifted by an additional factor that encodes the separation between their points of origin. Since the comoving distance is defined as the travel distance of light, this separation can be written in comoving coordinates as a difference of the distances to each source, leading to

an expression for the separation in redshift. Let's take the distance between them to be the sound horizon

$$r_s = r_2 - r_1 = \int_{t_1}^{t_2} \frac{dt}{a(t)} = \int_{z}^{z+\Delta z} \frac{dz'}{H(z')} \approx \frac{\Delta z}{H(z)}, \quad \Delta z \ll 1 \,. \tag{19}$$

In the parallel direction, the BAO feature measured as a separation in redshift is thus a measurement of $H(z)r_s$. The model for the Hubble parameter as a function of z is given by Equation 15 as

$$H(z)r_s = H_0 r_s \sqrt{\Omega_\Lambda + \Omega_k a^{-2} + \Omega_m a^{-3} + \Omega_r a^{-4}} \,. \tag{20}$$

These two quantities $D_A(z)/r_s$ and $H(z)r_s$ are the cosmological observables that can be probed by the BAO standard ruler observed in the transverse and parallel directions. Their evolution over redshift constrain the parameters $\{H_0, r_s, \Omega_m, \Omega_\Lambda, \Omega_r\}$ (Ω_k is not independent).

3 Measuring the BAO standard ruler with CHIME

3.1 BAO in the matter power spectrum

CHIME aims to measure the imprint of BAO on the large scale distribution of matter by surveying a significant fraction of the volume of the observable universe. The result of this survey will be a three-dimensional map of the density in neutral hydrogen within this volume. It is the statistics of this distribution that are of interest for cosmology, not the localization of any specific hydrogen cloud. In the standard model of cosmology, over and under-densities of matter are seeded by quantum fluctuations in the very early universe that result in a gaussian random field for the matter density $\rho(\mathbf{x})$ over space. Fractional deviations from the mean density $\bar{\rho}$

$$\delta_m = \frac{\rho - \bar{\rho}}{\bar{\rho}} \,, \tag{21}$$

are thus a zero-mean gaussian random field, which can be characterized entirely by an isotropic two-point correlation function

$$\xi(\mathbf{x}, \mathbf{x}') = \xi(|\mathbf{x} - \mathbf{x}'|) = \langle \delta_m(\mathbf{x}) \delta_m(\mathbf{x}') \rangle \,, \tag{22}$$

where the angle brackets denote an ensemble average over all of space. As time progresses, these over-densities grow under the influence of gravity, the dynamics of which can be described by perturbation theory to linear order as long as the over-densities remain small. Assessing the time and scale at which non-linearities become important will be addressed later in this work. As long as perturbations remain linear, Fourier modes evolve independently from one another, so it is common to work in Fourier space, with wavenumber $\mathbf{k}$ conjugate to position $\mathbf{x}$. The Fourier transformed density perturbations $\delta_m(\mathbf{k})$ are described by the power spectrum $P(\mathbf{k})$

$$\langle \delta_m(\mathbf{k}) \delta_m(\mathbf{k}')^* \rangle \equiv (2\pi)^3 P(\mathbf{k}) \delta^3(\mathbf{k} - \mathbf{k}'), \tag{23}$$

where

$$P(\mathbf{k}) = \int \mathrm{d}^3x \; \mathrm{e}^{i\mathbf{x}\cdot\mathbf{k}} \xi(\mathbf{x}, 0) \tag{24}$$

is the Fourier transform of the correlation function. Note that $P(\mathbf{k}) = P(k)$ since the correlation function is isotropic.

The most important data product CHIME will generate for cosmology is a measurement of the power spectrum of matter density perturbations $P(k_\perp, k_\parallel)$ (based on the neutral hydrogen tracer). The 3-d vector $\mathbf{k}$ in Fourier space is divided into components $k_\perp$ and $k_\parallel$ in the transverse and radial directions relative to the line of sight. We make this distinction to emphasize the nature of the measurements along those two directions. The power spectrum for $k_\perp$ is derived from angular separations on the sky, averaged azimuthally, whereas for $k_\parallel$ it corresponds to separations along the redshift (or frequency) direction. See Shaw et al. [19] for details on the planned power spectrum estimation program. The BAO feature as a series of harmonic peaks and troughs modulating the smooth broadband shape of the power spectrum – harmonic ringing associated with the peak in the correlation function at the primordial sound horizon. These "wiggles" are the Fourier-space analog to the BAO standard ruler, and can be used to infer cosmological distances as a function of redshift, and eventually constrain the Hubble constant H_0 and energy densities Ω_i. See Figure 3 in which a power spectrum/correlation function pair are plotted to demonstrate the correspondence between the peak at the BAO scale and the wiggles in the power spectrum.

Recall, in the transverse direction, the characteristic scale is encoded in the angular diameter distance to the sound horizon r_s, measured as an angular size $\Delta\theta$

$$D_A(z)/r_s = \frac{c}{r_s H_0 (1+z)} \int_0^z \frac{dz'}{\sqrt{1+\Omega_m[(1+z')^3-1]}} = \frac{1}{(1+z)\Delta\theta} \; , \tag{25}$$

and in the radial direction it is measured as a size in redshift Δz

$$H(z) r_s = H_0 r_s \sqrt{1+\Omega_m[(1+z)^3-1]} \approx \Delta z, \quad \Delta z \ll 1 \; , \tag{26}$$

(where a FRW geometry is assumed and energy density in radiation or curvature neglected for brevity).

The overall shape and amplitude of the observed power spectrum will differ from the underlying true spectrum due to effects such as redshift space distorsions, non-linear growth of structure, and bias from the 21 cm emission tracer, but the scale of the BAO feature is expected to be unaffected. This can be appreciated most clearly in real space, where it is difficult to imagine an astrophysical effect that could shift the centroid of the peak in the correlation function systematically over the entire survey volume. A careful treatment of this question can be found in Eisenstein et al. [6].

3.2 Fitting the power spectrum

Given an observation of the power spectrum $P_{obs}(k_\perp, k_\parallel; z)$ for a number of redshift bins, I'd like to derive $D_A(z)/r_s$ and $H(z)r_s$, from which I can constrain cosmological parameters as outlined in

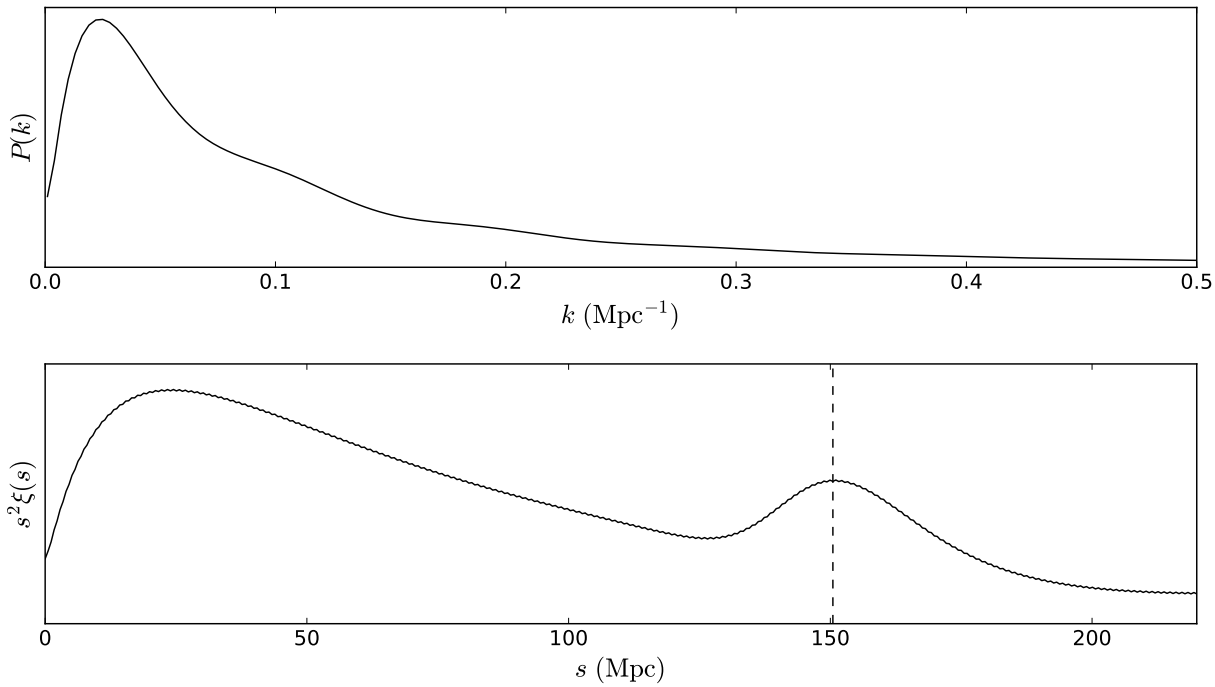

Figure 3: The matter power spectrum (top) at redshift $z = 2.5$, computed with CAMB [10], and the corresponding correlation function (bottom). The vertical dashed line indicates the scale of the BAO feature, which manifests itself as a bump in the correlation function. In Fourier space, this bump produces ringing – the wiggles that modulate the smooth shape of the power spectrum.

Section 2. The harmonic series of peaks and troughs that modulate the power spectrum correspond to the Fourier transform of an isolated feature in the correlation function localized at r_s. The oscillations in the power spectrum will therefore have a phase evolving like kr_s, i.e. the wavelength of the wiggles encodes the BAO scale. Varying the parameter r_s from its expected value will vary the separation in the BAO crests. This effect is illustrated in Figure 4, where many realisations of the power spectrum were computed using CAMB [10] for slightly different values of the cosmological parameters. Each spectrum has a slightly offset series of wiggles, but when the k axis is rescaled by the value of r_s calculated for the corresponding parameters, the wiggles line up again.

The quantities $D_A(z)$ and $H(z)$ are degenerate with r_s at any given redshift, for power spectra measured along the transverse and parallel directions respectively. In this way, the history of expansion can be compared to the theoretical expectation by the relative rescaling of the $P(k)$ wiggles as a function of redshift. Deviations from the fiducial model can be measured relative to $\tilde{D}_A(z)$ and $\tilde{H}(z)$, where the tilde denote the fiducial values of the parameters we would like to fit for. Define the rescaled $\tilde{k}$ for deviations from the fiducial parameters as

$$\tilde{k}_\perp = \frac{D_A}{\tilde{D}_A} k_\perp; \quad \tilde{k}_\parallel = \frac{\tilde{H}}{H} k_\parallel \,. \tag{27}$$

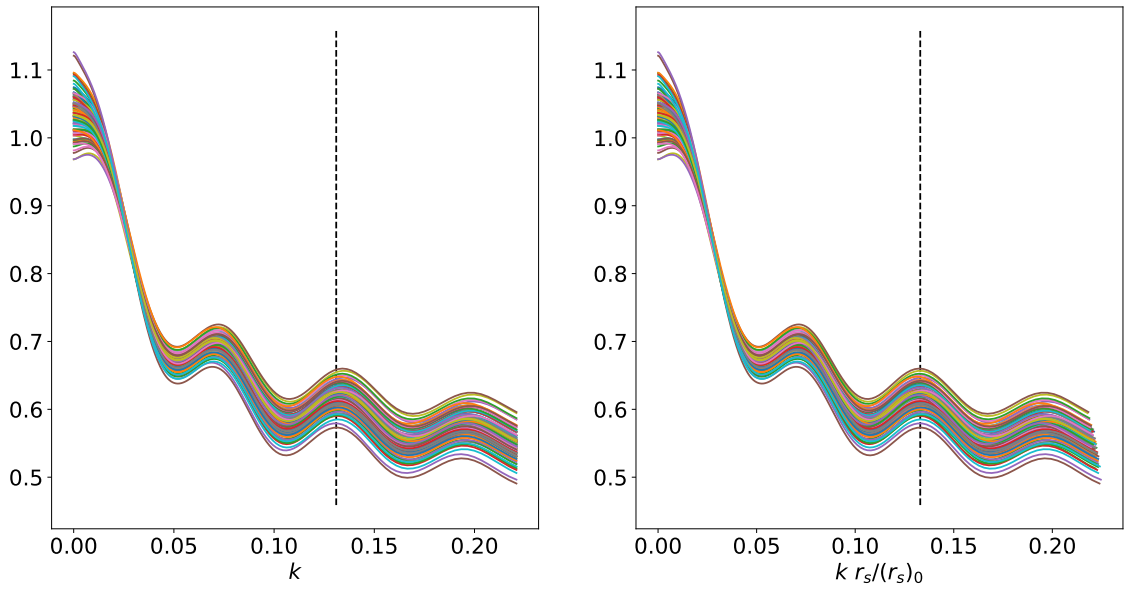

Figure 4: One hundred realisations of the power spectrum were computed with CAMB using different sets of cosmological parameters taken from an Monte-Carlo Markov chain from Section 5. These are plotted in the left panel to show that the different parameters produce harmonic series that are slightly offset. In the right panel, the same curves are shown, but with the k axis rescaled for every one by the sound horizon calculated for the corresponding parameters, realigning the wiggles. Note that the curves are the ratio to a power spectrum computed with low baryon density to emphasize the wiggles.

Since the shape of the power spectrum is well-constrained by theory and measurements of the CMB, it can be fit to the observations to extract these scaling factors at every redshift bin. The method I will adopt is to fit a fiducial power spectrum $P_{fid}[\tilde{k}_\perp(D_A), \tilde{k}_\parallel(H); z]$ computed from the current standard cosmological model (using the numerical solver CAMB [10]) that depends on D_A and H as parameters (through the $\tilde{k}$).

It is desirable to extract these quantities from the data in a way that is model-independent, to produce a simple processed dataset that can later be compared against model predictions. Model independence should be a significant advantage of working with a standard ruler, so it may appear surprising to employ a fiducial model and carry out the fitting process in Fourier space, for which a cosmology needs to be assumed. Localizing the peak in the correlation function might be a more straightforward approach to measuring the BAO, since the characteristic scale is encoded there in such an obvious way. However, even this approach requires some model-specific assumptions. To find the peak in the correlation function along the redshift direction, it is necessary to average over a large enough redshift range to resolve the BAO scale, and achieve high signal to noise. But the location of the peak is changing with redshift – the very effect we are attempting to measure – which will cause smearing of the peak and degrade the measurement. Accounting for this effect is done

by transforming the data from redshift into "real" space (i.e. in coordinates $\mathbf{x}$), an operation that requires a cosmology to be assumed. See Shaw et al. [19] for details.

In the end, the same limitation affects both methods, but working in Fourier space has other advantages. The effects of the evolution of structure over time are easier to separate from the signal in k-space, most importantly the onset of non-linearity, which first occurs on small scales (high k) and propagates to the larger scales over time. Since the BAO signal is damped with increasing k (for scales smaller than the diffusion length over the time until last scattering, thermal motions wash out the acoustic oscillation – Silk [20]), information at the tail-end of the spectrum will quickly be erased by non-linear evolution. To avoid contaminating the measurement with these polluted data, it is straightforward in Fourier space to restrict the range of k to values well-below the threshold of non-linearity. Procedures to undo some of this non-linear evolution and recover the BAO up to higher k have been developed, but for the purpose of forecasting, I will take a conservative approach overall and retain the simple hard cut. Where to set the upper limit on k will vary: lower redshifts will need a tighter cut-off value.

To determine k_{max}, I will adopt the criteria specified in Seo and Eisenstein [15], that the RMS of density perturbations averaged over a ball of diameter equal to the corresponding cutoff scale be one-half:

$$\sigma_R(z) = 0.5; \quad R = \frac{\pi}{2k_{max}} , \tag{28}$$

defined as

$$\sigma_R^2(z) \equiv \left\langle \left(\frac{3}{4\pi R^3} \int_{|\mathbf{x}|<R} \mathrm{d}^3x \; \delta_m(\mathbf{x},z) \right)^2 \right\rangle \propto \int_0^\infty \mathrm{d}k \; k^2 P(k) \, |f(kR)|^2 , \tag{29}$$

where $f(kR)$ is the Fourier conjugate to a 3-d tophat of radius R (see Weinberg 8.1.45). Taking $R \to \infty$, f becomes a δ-function and $\sigma_\infty = 0$, since over a large enough volume density fluctuations average out. If σ_R approaches unity, then there exist over or under-densities on the scale of R for which $\delta_m = \Delta\rho/\bar{\rho} \sim 1$, and linear perturbation theory breaks down. As matter collapses, these over and under-densities grow, such that this cutoff scale becomes larger. σ_R therefore tracks the evolution of the non-linear scale for density fluctuations.

Another consideration in fitting the power spectrum is that its broadband shape may deviate from the fiducial model. The measured power spectrum is of neutral hydrogen, which is expected to be a biased tracer of the overall matter density. The harmonics of the BAO should be robust to any bias – it is difficult to imagine any physical process that would systematically shift its location – but other features of the spectrum may look significantly different. An accurate measurement of the BAO should therefore be insensitive to anything but the wiggles. This can be achieved by parametrizing the broadband shape of the model power spectrum to isolate the information it carries. These nuisance parameters can then be marginalized over to remove their influence on the measurement. Seo et al. [17] explored a number of polynomial schemes for fitting the broadband shape and found that a fourth-order additive polynomial and a second-order multiplicative term are sufficient to remove the shape without introducing an excess of nuisance terms to the fit. The model

power spectrum that will be employed is

$$P_{mod}(k_\parallel, k_\perp) = P_{mod}(k) = B(k)P_{fid}(\tilde{k}) + A(k) \tag{30}$$

$$A(k) = a_0 + a_1 k + a_2 k^2 + a_3 k^3 + a_4 k^4 \tag{31}$$

$$B(k) = b_0 + b_1 k + b_2 k^2 \,, \tag{32}$$

where P_{fid} is the power spectrum calculated for a fiducial cosmology and used as a template to fit the BAO feature. The power spectrum is modelled as isotropic, with no individual dependence on the components $k_\parallel, k_\perp$, since no anisotropy is expected in the data that cannot be accounted for in the analysis. The dependence on D_A and H is encoded in the $\tilde{k}$ as indicated in Equation 27.

4 Fisher forecast of errors on D_A and H

4.1 Fisher information matrix overview

A useful tool for forecasting errors on an upcoming measurement is the Fisher Information Matrix (FIM). For observations $P_{obs}(\mathbf{k})$ over some domain in $\mathbf{k}$ and a model $P_{mod}(\mathbf{k};\alpha_i)$ with parameters α_i, the log-likelihood of the model given the data is

$$\ln \mathscr{L}(\alpha) = -\frac{1}{2}\sum_{ij}(P_{obs}(\mathbf{k}_i) - P_{mod}(\mathbf{k}_i))\Sigma^{-1}_{ij}(P_{obs}(\mathbf{k}_j) - P_{mod}(\mathbf{k}_j)) \,, \tag{33}$$

where Σ_{ij} is the covariance between data-points i and j.

The FIM is defined as the curvature of the log-likelihood in parameter-space

$$\mathscr{F}_{\alpha\beta} = -\left\langle \frac{\partial^2 \ln \mathscr{L}}{\partial\alpha\partial\beta} \right\rangle = \sum_{ij} \frac{\partial P_{mod}(\mathbf{k}_i)}{\partial\alpha} \Sigma^{-1}_{ij} \frac{\partial P_{mod}(\mathbf{k}_j)}{\partial\beta} = \left(\frac{\partial P}{\partial\alpha}\right)^T \Sigma^{-1} \left(\frac{\partial P}{\partial\beta}\right) , \tag{34}$$

where in the last expression the subscripts have been suppressed and the sum is represented as a matrix multiplication. Note that data does not appear in this expression, only the data covariance matrix Σ carries information about the measurement procedure. If the model is linear in the parameters – $P_{mod} = f^T\alpha$ for some basis f – the likelihood is a gaussian centred on the true values $\hat{\alpha}$ (denoted now as a vector)

$$\begin{aligned} \ln \mathscr{L}(\alpha) &= -\frac{1}{2}(\alpha - \hat{\alpha})^T f\, \Sigma^{-1}\, f^T(\alpha - \hat{\alpha}) \\ &= -\frac{1}{2}(\alpha - \hat{\alpha})^T \Pi^{-1}(\alpha - \hat{\alpha}) \,, \end{aligned} \tag{35}$$

and the inverse covariance of the parameters corresponds exactly to the FIM: $\mathscr{F}_{\alpha\beta} = (\Pi^{-1})_{\alpha\beta}$.

For a model that is an arbitrary function of the parameters, $P(\alpha)$, the FIM corresponds to the

first term in a Taylor expansion around the true values

$$\ln \mathscr{L}(\alpha) \approx -\frac{1}{2}(\alpha-\hat{\alpha})^T \left(\frac{\partial P}{\partial \alpha}\Big|_{\hat{\alpha}}\right)^T \Sigma^{-1} \left(\frac{\partial P}{\partial \alpha}\Big|_{\hat{\alpha}}\right)(\alpha-\hat{\alpha}) \; . \tag{36}$$

It can further be shown that the inverse of the FIM sets a lower bound on the covariance of the parameters (the Cramr-Rao bound): $\Pi_{\alpha\beta} \geq (\mathscr{F}^{-1})_{\alpha\beta}$. The FIM can thus be employed as a forecast for the errors on the model parameters, with an estimate of the data covariance based on the design of the instrument, and assuming the parameter estimation is performed in a near-optimal way.

4.2 S/N for CHIME power spectrum measurements

To proceed with error estimation using the Fisher matrix formalism of the previous section, derivatives of the model power spectrum must be evaluated. Those for the polynomial coefficients are straightforward, but the dependence on the parameters of interest $D_A(z)$ and $H(z)$ must be arrived at through the components of $\tilde{\mathbf{k}}$

$$\frac{\partial P}{\partial \alpha} = \frac{\partial P}{\partial \tilde{k}}\frac{\partial \tilde{k}}{\partial \alpha} = \frac{\partial P}{\partial \tilde{k}}\frac{\partial}{\partial \alpha}\sqrt{\left(\frac{D_A}{\tilde{D}_A}\right)^2 k_\perp^2 + \left(\frac{\tilde{H}}{H}\right)^2 k_\parallel^2} \tag{37}$$

$$= \begin{cases} \frac{1}{D_A}\frac{k_\perp^2}{k}\frac{\partial P}{\partial k}, & \alpha = D_A \\ -\frac{1}{H}\frac{k_\parallel^2}{k}\frac{\partial P}{\partial k}, & \alpha = H \; , \end{cases} \tag{38}$$

where in the last step, I have evaluated the expression at the fiducial values $\tilde{D}_A = D_A$, $\tilde{H} = H$. The full set of derivatives that appear in the Fisher matrix for the power spectrum model given in Equation 30 are

$$\frac{\partial P}{\partial D_A} = \frac{1}{D_A}\frac{k_\perp^2}{k}\frac{\partial P}{\partial k} \qquad \frac{\partial P}{\partial a_n} = k^n$$

$$\frac{\partial P}{\partial H} = -\frac{1}{H}\frac{k_\parallel^2}{k}\frac{\partial P}{\partial k} \qquad \frac{\partial P}{\partial b_n} = k^n P(k) \; ,$$

with all values from the fiducial model, and n spanning the set of polynomial coefficients.

The remaining component of the Fisher matrix calculation is the covariance for the observed power spectrum $P_{obs}(k_\perp, k_\parallel; z)$. It can be estimated from models of the instrumental response to the expected signal. Seo et al. have carried out this forecasting calculation for a generic transit interferometer hydrogen intensity survey that can be evaluated for the CHIME specifications. Signal to noise, S/N, is calculated for every discrete bin in three-dimensional k-space within which the power spectrum is to be estimated. The volume of such an element is

$$\mathrm{d}k_\parallel \, \mathrm{d}^2 k_\perp = 2\pi k_\perp \, \mathrm{d}k_\perp \, \mathrm{d}k_\parallel \; . \tag{39}$$

For a survey volume V_{sur}, bandwidth Δf, and integration time t_{int}, they find a signal to noise ratio of

$$\frac{\mathrm{S}}{\mathrm{N}} = \sqrt{\frac{2\pi k_\perp \, \mathrm{d}k_\perp \, \mathrm{d}k_\parallel V_{sur}}{2(2\pi)^3}} \frac{P_{HI}(k_\perp, k_\parallel)\hat{W}^2}{P_{HI}(k_\perp, k_\parallel) + \left[\frac{g\bar{T}_{sky} + \bar{T}_a}{g\bar{T}_{sig}\sqrt{t_{int}\Delta f}}\right]^2 V_R + N_{shot}} \,. \tag{40}$$

$P_{HI}(k_\perp, k_\parallel)\hat{W}^2$ is the power spectrum for neutral hydrogen – the signal we wish to detect – weighted by a window function to account for the instrumental response at the corresponding $k_\perp, k_\parallel$. The prefactor multiplies the signal to noise by the square root of the number of modes averaged in that k-space bin; the first term in the denominator is sample variance, the second is receiver and foreground noise (V_R is the pixel volume; this expression is derived in the paper), and the last term is galactic shot noise. Since CHIME does not resolve individual galaxies, N_{shot} is set to zero in what follows. Finally, the integration time is set to 5 years, the nominal operation time for CHIME.

Richard Shaw has implemented this calculation for the CHIME instrument in a public code hosted at https://github.com/jrs65/neutrino-forecast. I have branched off the code to compute the signal to noise in the observed power spectrum and also return the fiducial power spectrum itself and its derivative. The window function $\hat{W}(k_\perp, k_\parallel)$ was defined as a sinc function in the parallel direction and a triangle function in the perpendicular direction. The sinc function is the Fourier transform of a top-hat, which is the transfer function used along the frequency direction to divide it into bins. Instrumental response along the $k_\perp$ direction is determined by the sensitivity to different angular scales achievable using the interferometric array. For a compact, redundant interferometer like CHIME, this window function turns out to be a triangle, bounded by the angular scale corresponding to the longest baseline of the array. Details are provided in Seo and Hirata [16]. These choices for the window function are a simplification. The real instrumental response will necessarily be more complicated, but refinement of this aspect of the analysis will be left for future work.

To accurately model the signal to noise, redshift space distorsions (RSD) are included in the neutral hydrogen power spectrum $P_{HI}(k_\perp, k_\parallel)$, introducing anisotropy between the $k_\perp$ and $k_\parallel$ directions. RSD are modelled by the widely used approximation introduced by Kaiser [9], modulating the power spectrum with a factor

$$(b + \mu^2 f)^2; \quad \mu = \frac{k_\parallel}{k} \,, \tag{41}$$

where f is a function that tracks the growth of perturbations over cosmic time and $b = \delta_{HI}/\delta_m$ is a bias term to account for the fact that the overdensity in neutral hydrogen may not be exactly equal to the overdensity in matter (see Dodelson [5] chapter 9.4). For the purpose of forecasting, I set $b = 1$. After estimating the signal to noise, this effect is removed from the power spectrum, restoring its isotropy so it can be used as the template $P_{fid}(k)$ for the fitting function. This reflects the expected procedure for analysis of measured data.

The $(k_\perp, k_\parallel)$ grid for which forecast errors are generated is set by the cut-off k_{max} determined at every redshift from the expected onset of non-linear evolution (as prescribed in Section 3.2), and a choice for the number of uniformly spaced bins across the range. The length of one wiggle in the power spectrum is about 0.05 Mpc^{-1}, so a resolution of 0.01 Mpc^{-1} should be amply sufficient

z	k_{max}/h	D_A/r_s	σ_{D_A}	Hr_s	σ_H	ρ_{H,D_A}
2.16	0.568	11.66	0.069 (0.59 %)	0.1095	0.00074 (0.68 %)	-50.24 %
1.58	0.426	11.92	0.043 (0.36 %)	0.0832	0.00037 (0.45 %)	-58.38 %
1.18	0.328	11.66	0.039 (0.33 %)	0.0672	0.00031 (0.46 %)	-55.80 %
0.89	0.255	10.96	0.059 (0.53 %)	0.0567	0.00044 (0.77 %)	-41.50 %

Table 1: Errors on D_A/r_s and Hr_s from the Fisher matrix. ρ_{H,D_A} is the correlation coefficient of the errors.

to Nyquist sample the BAO feature. The sampling of $k_\parallel$ will determine the maximum number of redshift bins that can partition the full frequency band while still spanning large enough scales to achieve that resolution. This is analogous to the familiar case of a time-domain discrete Fourier transform for which the frequency resolution is given by the inverse of the total time spanned by the sample: $\Delta f = 1/t$. The bounds of the redshift bins and the respective values of k_{max} used in this work can be found in Table 1

The signal to noise estimated in this way is displayed in Figure 5 for two redshift bins located in different regions of the CHIME band. In these figures, the cut above k_{max} has not been enforced. Comparison of the two panels shows how the sensitivity of the instrument across $k_\perp$ changes with redshift, mainly due to the decreasing angular resolution with increasing redshift, which corresponds to increasing wavelength. Thus the high k region of the spectrum can be probed with high signal to noise at lower redshifts, which is just when it becomes increasingly polluted with non-linearities. For the high redshift bin, 64% of the signal to noise is located within the non-linear cut-off, but this drops to only about 3.5% in the low redshift case. These competing trends are inherent to any hydrogen intensity survey, and provide a strong motivation to investigate methods for recovering the information at these higher k. Some of the non-linear evolution can be modelled and corrected for using the method of Lagrangian displacements, based on the Zel'dovich approximation, as described in Eisenstein et al. [6]. Integrating this method into the present sensitivity forecasts will be left for future work.

4.3 Results

The Fisher matrix for errors on $D_A(z)$ and $H(z)$ can now be evaluated given the signal to noise forecast derived in the previous section. The fiducial cosmology I use here is standard ΛCDM, with values for the cosmological parameters taken from the TT,TE,EE+lowP+lensing+ext likelihood fits of Planck 2015 [13]. The power spectrum for this fiducial model is computed using the software package `Cora` [18]. Table 1 lists the derived errors and the fiducial values of the distance measures for every redshift. Note the large correlation coefficient between D_A and H. This is to be expected given the nature of the measurement, for which most data points represent some combination of $k_\perp$ and $k_\parallel$, so the two parameters are not determined independently.

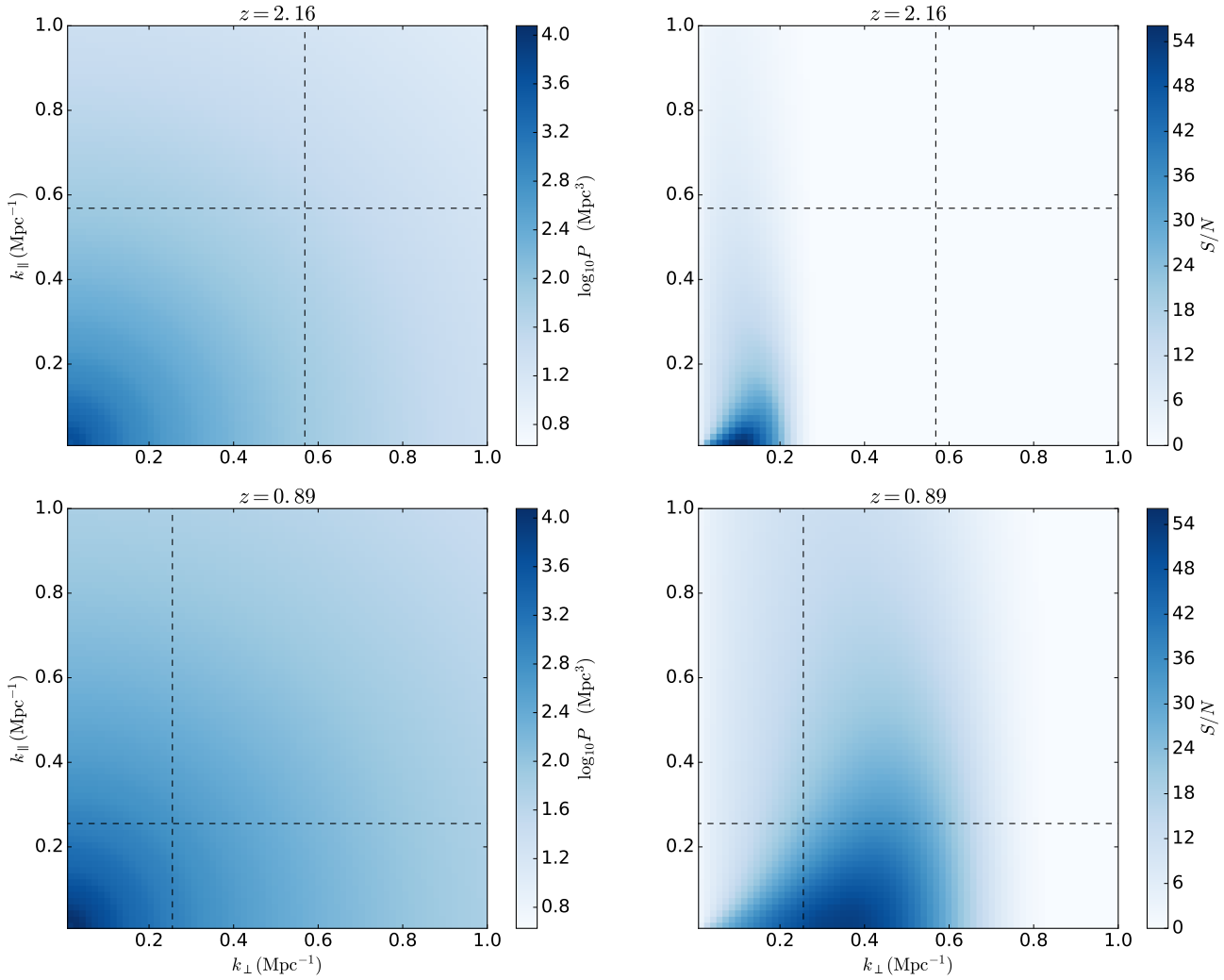

Figure 5: Forecasted CHIME HI power spectrum measurement (left column) and signal to noise ratio (right column) for highest (top row) and lowest (bottom row) redshift bands used for this analysis. The dashed lines indicate the scale chosen as the cutoff beyond which non-linear evolution becomes important, based on Equation 28

5 Parameter sensitivity forecasts

In the previous sections, the necessary machinery has been established in order to proceed to parameter sensitivity forecasts. Equations 17 and 20 provide the model predictions for the observables $D_A(z)$ and $H(z)$, with parameters $\{H_0, r_s, \Omega_m, \Omega_k, \Omega_r\}$. Note that Ω_Λ is not included since it is determined by the other three (Equation 14). The energy in radiation is negligible at late times ($\Omega_r \sim 10^{-4}$, with at most $(1+z)^4 \sim 10^2$) compared to the other constituents, so it will have little incidence on the fits. The temperature of the CMB has been measured to extremely high precision and as a result uncertainties on $\Omega_r h^2$ are negligible. I will simply take them to be zero in the likelihood, fixing Ω_r. H_0 and r_s are manifestly degenerate – some prior knowledge of r_s will be necessary

to set any constraints on the Hubble constant. The most precise estimates of the sound horizon are from measurements of the CMB, which is what is typically used to break this degeneracy in BAO observations. However, in the context of apparent tension between CMB and distance ladder measurements of H_0, it will be interesting to estimate the precision of constraints from CHIME BAO alone, independent of the CMB and in general without assuming flatness. Another handle on the sound horizon can be obtained from measurements of the primordial deuterium abundance and modelling of the early universe nucleosynthesis.

5.1 Determining r_s from primordial deuterium abundance

The predictions from the theory of Big Bang nucleosynthesis for the abundances of light elements in the universe is one of the pillars of modern cosmology. Starting with minimal assumptions about a universe that started with a Big Bang – homogeneity and isotropy, that physics was described by the same laws at early times as it is today – the principles of thermodynamics and nuclear physics make definite predictions for the relative abundances of helium and deuterium that condense out of the primordial plasma as it cools. Observations of the helium fraction in low metallicity stars have confirmed these predictions to remarkable accuracy [12]. The relic abundance of deuterium is determined by the efficiency of the reaction that converts it to helium: D + p $\leftrightarrow$ ^{3}He + γ, which in turn depends on the physical density of baryons $\Omega_b h^2$. A higher density would have allowed more deuterium to be produced before expansion brought the reaction to a halt. This makes the deuterium abundance relative to hydrogen, D/H, a sensitive probe of $\Omega_b h^2$. Following Addison et al. [1] I will use the value derived from observations of the absorption spectra of high-redshift quasars by Cooke et al. [4], in their most recent publication:

$$\Omega_b h^2 = 0.02235 \pm 0.00037\,. \tag{42}$$

A prior on $\Omega_b h^2$ is sufficient to break the H_0–r_s degeneracy because the sound horizon of BAO is determined largely by Ω_b and Ω_m. Evaluating the integral in Equation 1 cannot be done analytically in general, but fitting formulae have been derived that are accurate in restricted regions of parameter space. Aubourg et al. [3] provide a formula for the sound horizon at the drag epoch, numerically calibrated from the linear perturbation code CAMB [10]

$$r_s \approx \frac{55.154 \exp[-72(\omega_\nu + 0.0006)^2]}{(\Omega_m h^2)^{0.25351} (\Omega_b h^2)^{0.12807}}\ \text{Mpc} \approx \frac{55.154}{(\Omega_m h^2)^{0.25351} (\Omega_b h^2)^{0.12807}}\ \text{Mpc}, \tag{43}$$

where $\omega_\nu \equiv 0.0107(\sum m_\nu / 1.0\text{eV}) \leq 0.006$ is a correction for non-zero neutrino mass. Investigating the effects of neutrino masses or additional relativistic species is outside the scope of this work, so I will fix $\omega_\nu = 0$. Given the limit set by Planck, $\sum m_\nu \leq 0.6eV$, this results in $< 0.5\%$ variation in the value of r_s. Aubourg et al. [3] quote an accuracy of 0.021% compared to the numerical solutions.

5.2 Parameter estimation

Adopting this scaling relation for r_s removes it as a free parameter from the model for $D_A(z)$ and $H(z)$ in favour of $\Omega_b h^2$. The full set of fitting parameters I will consider for the ΛCDM model is $\{H_0, \Omega_b, \Omega_m, \Omega_k\}$. Uniform priors on all of these will implicitly be assumed with the exception of the combination $\Omega_b h^2$, for which the gaussian standard deviation is given in Equation 42. The likelihood of the data will be approximated as $\mathrm{e}^{-\chi^2}$, with the errors estimated from the sensitivity forecasts of Section 4. The posterior probability density for the parameters is given by Bayes' theorem

$$P(H_0, \Omega_b, \Omega_m, \Omega_k) \propto \mathrm{e}^{-\chi^2} P(\Omega_b h^2) \; . \tag{44}$$

Evaluating the posterior is most conveniently performed with the Monte Carlo Markov Chain method, a widely used stochastic algorithm for sampling the probability distribution. It produces a cloud of points in parameter space with a number density proportional to the distribution. This method is advantageous for exploring large-dimensional spaces since its computational expense scales like the number of points in the chain for any number of parameters, whereas evaluating the likelihood on an explicit grid grows to the power of the number of dimensions. Additionally, analyzing the statistics of the posterior distribution is very straightforward since the Markov chain produces a representative sample from which it is trivial to compute the moments.

5.3 Constraining H_0

Different models and datasets will be considered to evaluate the performance of the CHIME survey for estimating H_0 and distinguishing between variations on the cosmological model. The only extension I will consider to ΛCDM is a deviation from cosmological-constant dark energy. The evolution of the dark energy is determined by its equation of state,

$$p_{de} = w \rho_{de} \; , \tag{45}$$

relating density and pressure, parametrized by the constant w. Λ has $w = -1$. For comparison, $w = 0$ for pressureless matter and $w = 1/3$ for radiation. For values of $w \neq -1$, dark energy no longer has constant density throughout the expansion of space, i.e. Equation 15 must be modified to include some power of the scale factor multiplying Ω_Λ.

Constraints using priors from measurements of the CMB will be considered separately to get an idea of the precision achieved by combining these complimentary observations, assuming they are found to be consistent. In what follows I will use 'CHIME' to refer to the sensitivity forecasts estimated in this work, 'D/H' to indicate a prior on $\Omega_b h^2$ from Cooke et al. [4], 'CMB' to indicate priors on $(\Omega_b h^2, \Omega_m h^2)$ from the Planck 2015 parameter fits [13], and 'w' when deviations from the cosmological constant are allowed. The resulting marginalized 68% confidence intervals on H_0 for all of these combinations are summarised in Table 2.

Table 2: Marginalised 68% confidence intervals quoted as a relative 1σ deviation on the mean for the parameter H_0.

CHIME+D/H	CHIME+CMB	CHIME+D/H+Ω_k	CHIME+D/H+w	CHIME+CMB+w
0.44%	0.39%	1.02%	2.66%	0.83%

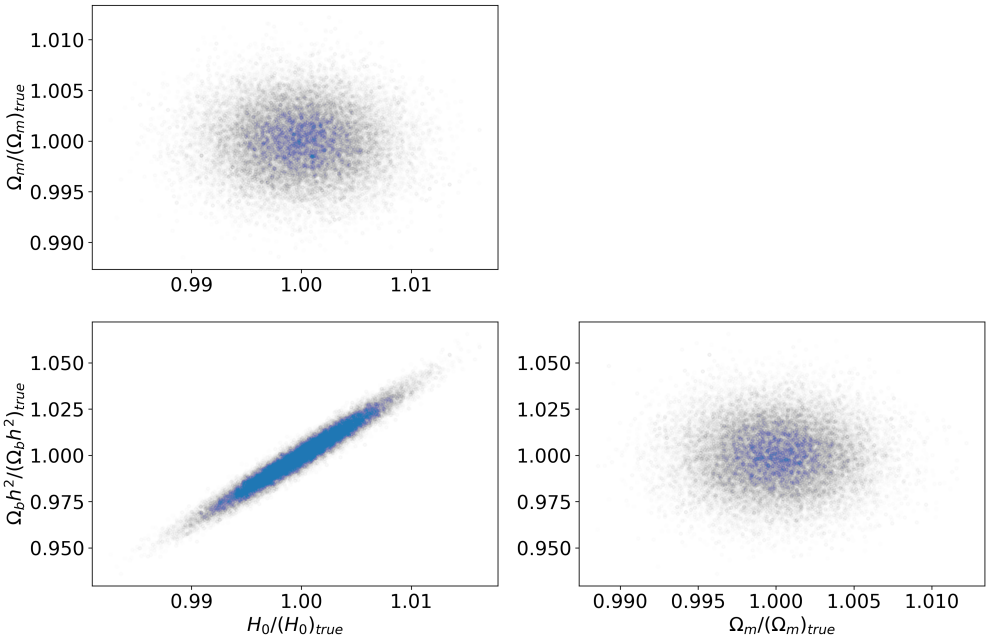

Figure 6: MCMC chains as parameter constraints for CHIME+D/H with a model with fixed curvature.

CHIME+D/H This is the minimal ΛCDM model favoured by observations so far. Curvature is fixed at the negligible value obtained in Planck 2015, $\Omega_k = 0.04 \pm 0.040$ [13]. A corner plot of the MCMC posterior distributions for the parameters is shown in Figure 6. The contraints on $\Omega_b h^2$ appear to reproduce the input prior. This shows that CHIME BAO measurements are not particularly sensitive to the baryon density. The constraining power is confined to the H_0–Ω_m plane. Marginalising over Ω_m results in a 0.44% standard deviation, competitive with the CMB-derived measurements and many times more precise than distance ladder estimates.

CHIME+D/H+Ω_k Next, we can relax the assumption of an essentially flat universe to see how this affects the CHIME constraint. In this fit, Ω_k is a free parameter, with a uniform prior. The resulting posterior on Ω_k spans roughly ± 0.1, well beyond any plausible curvature based on all observations to date. Nevertheless, the CHIME sensitivities produce constraints of 1.02% on H_0. This reflects the fact that over such a broad range of redshift, measurements of the Hubble constant from BAO

are not degenerate with curvature, reinforcing their complimentary nature to CMB observations.

CHIME+D/H+w Now we go beyond ΛCDM, allowing values of $w \neq -1$. This adds considerably more freedom to the model, resulting in errors of $\sim 2.7\%$ on H_0. The chains extend about ± 0.2 around $w = -1$, as can be seen in the corner plot in Figure 7.

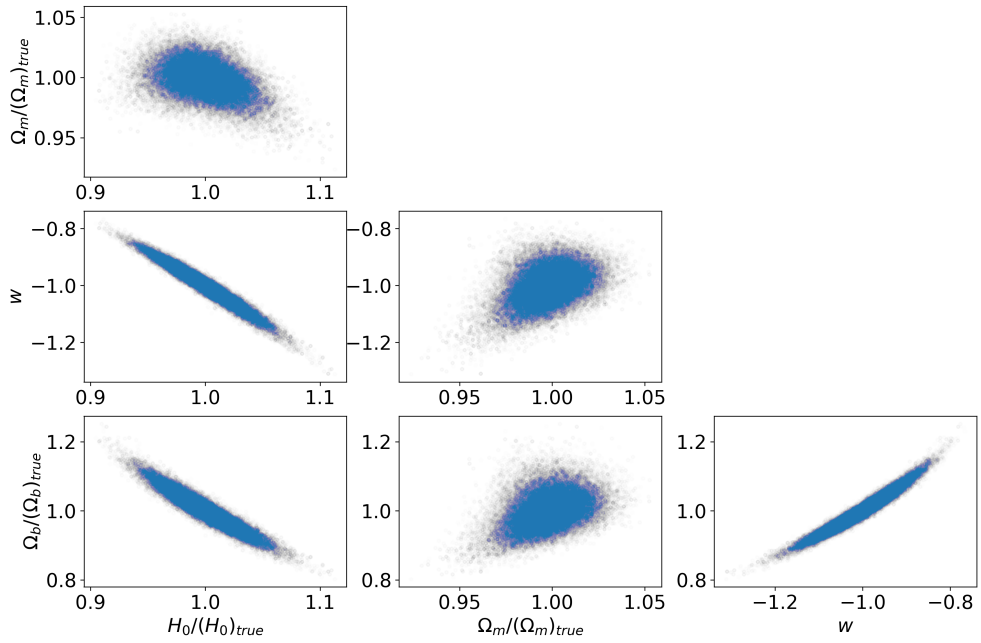

Figure 7: MCMC chains as parameter constraints for CHIME+D/H with a model where $w \neq -1$ is free.

CHIME+CMB Observations of the CMB constrain the baryon and matter densities very precisely. In this fit, gaussian priors on $\Omega_b h^2$ and $\Omega_m h^2$ are included. The 68% confidence limits on the parameters quoted in Planck 2015 are used as standard deviations for these priors. This should be a good approximation since there is little covariance between these parameters in the CMB fits, as can be seen in Figure 6 of Planck 2015 [13]. The CMB priors improve the derived constraint on H_0 slightly, mainly as a result of including any prior on Ω_m at all, since the measurement of $\Omega_b h^2$ from Cooke et al. [4] is competitive with the CMB precision.

CHIME+CMB+w The inclusion of the same CMB priors in the free w fit has a much more significant effect, as can be seen by comparing the parameter constraints shown in Figures 8 and 7. BAO from CHIME together with CMB can measure H_0 to $\sim 1\%$ accuracy even with $w \neq -1$.

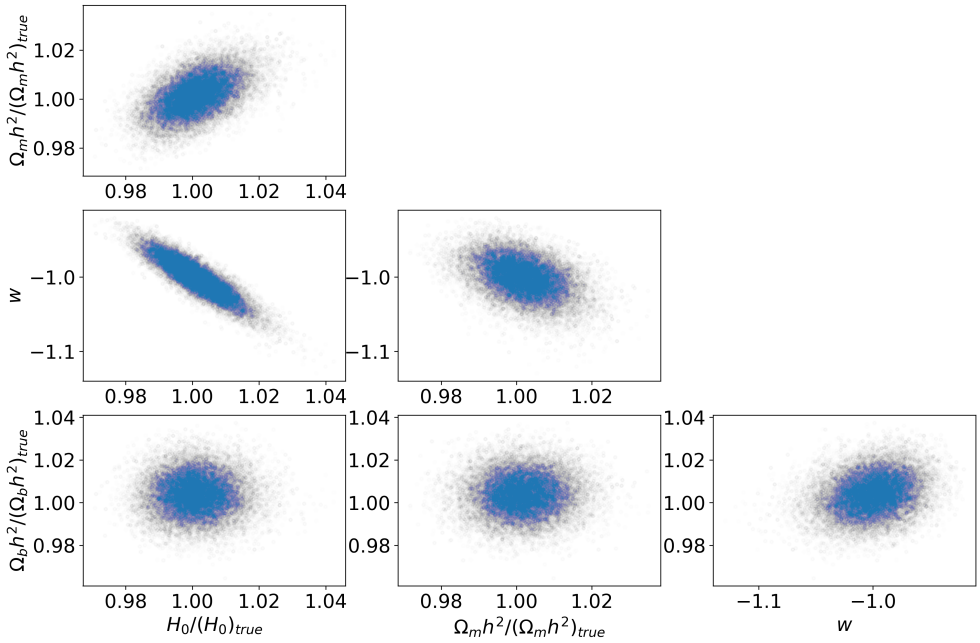

Figure 8: MCMC chains as parameter constraints for CHIME+CMB with a model where $w \neq -1$ is free.

5.4 Constraining w

Although it is not the main focus of this work, measuring w with high precision is the primary motivation for CHIME. It is therefore worth taking a moment to note the sensitivity forecasts obtained on w. Figure 9 shows contours for the posterior in the H_0–w parameter plane. Two cases were considered: setting a prior on the baryon density from deuterium abundance or priors on the baryon and matter densities from CMB observations. The CMB prior is much more constraining than deuterium since it includes $\Omega_m h^2$. This is because w determines the power of the scale factor with which the weight of dark energy evolves when calculating the Hubble parameter, Equation 20, where the matter density appears in a similar role. The measurement of $\Omega_m h^2$ from the CMB breaks this degeneracy and allows for constraints at the 2.5% level on w, whereas CHIME+D/H produce errors around 6.8%..

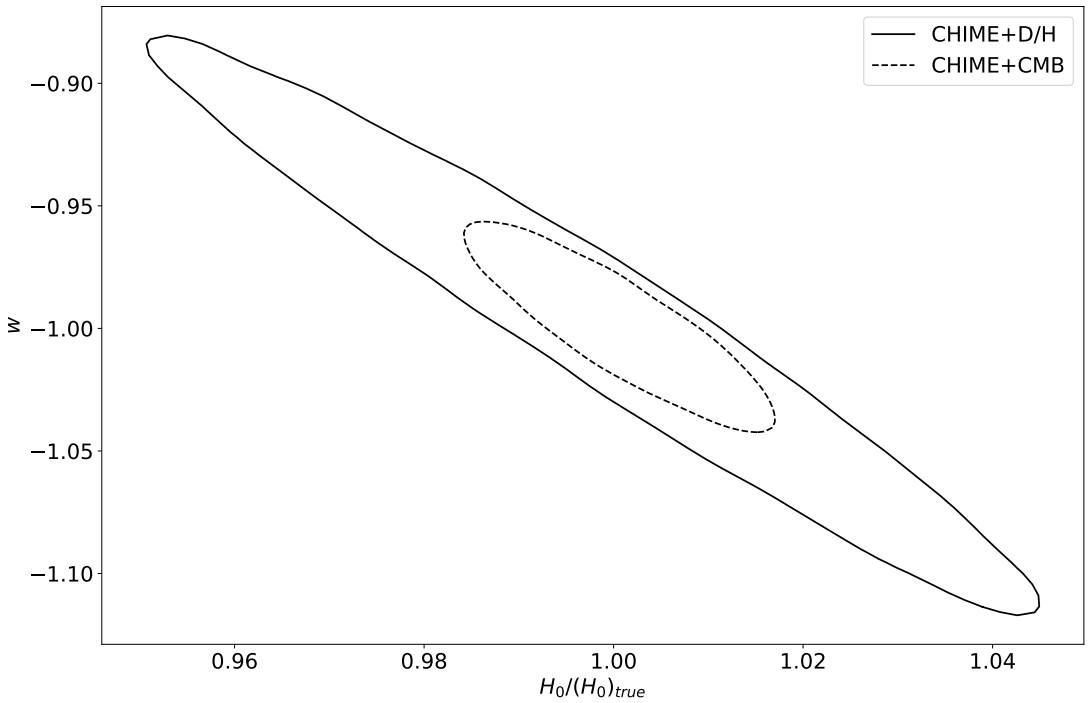

Figure 9: 68% confidence regions for w and H_0 based on the forecasted CHIME sensitivity. In one case a prior on $\Omega_b h^2$ from deuterium abundance is included and in the other it is priors on both $\Omega_b h^2$ and $\Omega_m h^2$ from measurements of the CMB.

Commissioning CHIME

In the introduction, I gave a brief description of the Canadian Hydrogen Intensity Mapping Experiment (CHIME), the telescope which has been at the center of my master's work. Over the past two years, CHIME has been undergoing the final stages of commissioning, leading up to a ceremonial first light in the fall of 2017 followed shortly by the beginning of data acquisition in spring 2018. This represents the culmination of years of effort from a group of researchers scattered mostly between the main partner institutions at McGill, the University of Toronto, and the University of British Columbia. In this chapter, I will focus on my individual (not single-handed!) contributions to the project as a master's student. Given the scale and complexity of the instrument, these have been miscellaneous and provided the opportunity to practice wielding a wide range of tools and ideas. As such, I will not try and provide a narrative here, and the following contributions will be presented in no particular order.

1 FLA power control

The last stage of the analog chain that spans from the antenna feeds to the digitizer at the input of the correlator is a filter amplifier (FLA). In addition to amplifying the signal to the appropriate level for optimal digitization, this component applies a 400-800 MHz spectral bandpass filter. Effective filtering is crucial to the fidelity of the digitization because the latter operates by alias sampling. The signal is sampled at 800 MHz – only half the Nyquist rate – which causes aliasing of the 400-800 MHz band into 0-400 MHz. Since this frequency range is cleared by the FLA, there is nothing to confuse the aliased signal, and no information is lost. The FLA also provides a DC level on the transmission line to power the upstream amplifiers.

CHIME has 2048 feeds, and thus 2048 signal chains. With such a large number of components, there are bound to be failures and these can be disruptive to the operation of the instrument. An oscillating amplifier can produce loud radio frequency interference (RFI) that will contaminate the channels near it for example. To mitigate this issue, it is desirable to have control over the power going to individual FLA, so that they can be shut down without disrupting the rest of the system. It is also useful to have the ability to query and record the FLA power state over time, to monitor the system and inform later data analysis. These considerations led to the development of an FLA power control module, including hardware and software components. Kwinten van Gassen, a student researcher at UBC, led the development of these tools and I contributed to their physical in-

stallation and subsequent feature updates necessary to integrate them into the full CHIME software framework.

1.1 Hardware installation

The receiving and frequency channelization component of the CHIME correlator is housed in two RF shielded rooms, themselves embedded in repurposed shipping containers – one collects signals from two cylinders. The coaxial cables carrying the signal interface with the RF room via a brass bulkhead through which the FLA ports protrude. The installation procedure involved drilling holes in this bulkhead to mount the FLA support rack and to allow the FLA connectors through, cleaning the brass surface to ensure good electrical contact and prevent RFI leakage, inserting the FLA in the bulkhead and connecting them to the power distribution system while recording their serial numbers and location, and bolting them into place with the appropriate torque to ensure no gaps in the conducting surface. These steps were repeated for all 2048 amplifiers.

The power distribution is divided between control boards that can provide power to 16 FLA. Each output can be toggled by a photoelectric relay, and groups of 8 relays are set by sending a byte to the corresponding individually addressed controller chip over the Inter-integrated circuit (I2C) protocol. Power control boards are grouped into buses that share a data line, with 16 addresses (8 boards) on each line. Instructions are sent over the buses by an Arduino-based module. Each module controls four buses and has a persistent state, i.e. it will restore the power state of the array of FLA if it is power-cycled. In all, there are 4 modules with 4 buses (16 branches) each with 16 addresses (256 branches) that control 8 FLA (2048 branches). The modules are powered by the same source as the FLA themselves, so that when the underlying power supply is powered on or off the state of the FLA is restored automatically.

I helped to install and cable up the modules and power supply in the receiver room. One power supply provides constant voltage to 1024 FLA, with a total output of around 2 kW at roughly 300 A. This current is carried by eight heavy-duty copper cables strung across the ceiling. The Arduino modules interface over USB with a ‘housekeeping’ PC that runs the control software which I will describe in the following section. The photograph in Figure 10 shows the inner FLA bulkhead.

1.2 Software development

The Arduino-based modules that communicate over I2C with the power control boards are managed through a software package written in Python. The software wraps an I2C client into abstract objects representing the bulkheads, power boards, and individual FLA locations. It was developed initially by Kwinten van Gassen, with a command line interface for user interaction. Later, it was decided that CHIME would adopt the Representational state transfer (REST) standard interface for system monitoring and control, so it was necessary to write a new interface to the FLA control software. REST operates over the HTTP protocol so this involved building a web server that could be run on the housekeeping PC and listen for commands from users over HTTP. I also put together a command line interface to the REST server for convenience.

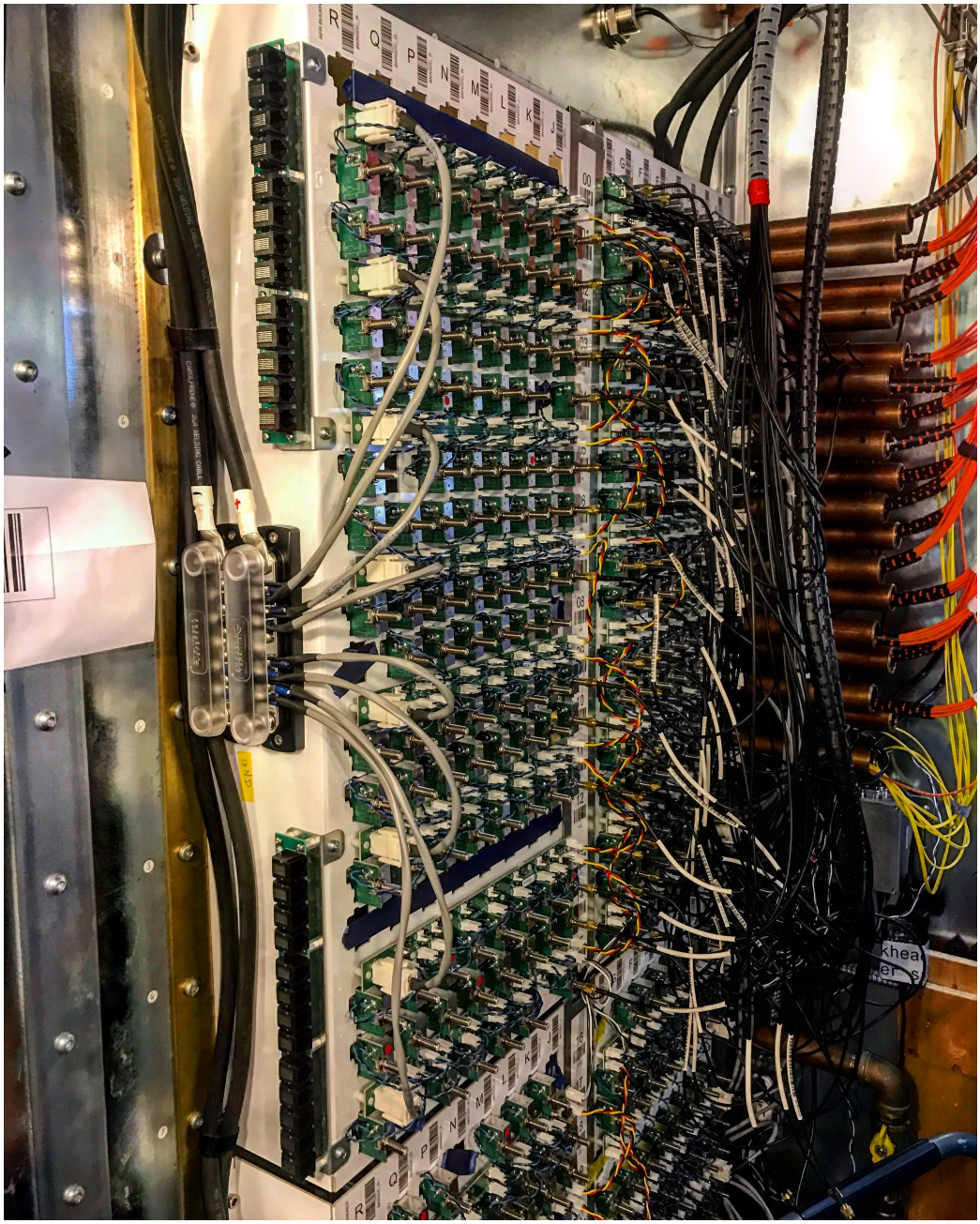

Figure 10: Installed FLA bulkhead. The FLA themselves are housed in the metallic boxes with SMA ports protruding from the white support rack. The power control boards are the green circuit boards mounted horizontally between rows. (Photo taken by Mohamed Shaaban.)

2 Receiver software development

The full data rate output by the CHIME correlator is almost 135 TB per day, in a stream of 2048×2048 visibility matrices for 1024 frequencies generated every 10 s. Capturing and processing this data to write it to disk for later analysis is not a trivial task, especially since it needs to be performed in real time to maintain a continuous acquisition over a period of months. The receiver software pipeline that handles the data flow from the correlator is divided into multiple stages, distributed between different machines but all under a common software framework built in `C++` named `kotekan`.

The 'X'-engine of the correlator receives the stream of frequency channelized data from the 'F'-engine for every one of the 2048 inputs. It is made up of 256 nodes, each with 4 GPUs, such that every GPU receives the data from all inputs for a single frequency. The inputs are multiplied and integrated to produce the visibility matrix and then passed on to the `kotekan` pipeline. The first stages of the pipeline occur on the GPU nodes themselves, but the 256 data streams need to be collected before they can be written out and archived. This happens on two dedicated receiver nodes, networked to the GPU array over 40 GbE links. The data files written out by the receiver nodes finally need to be compressed and copied over to an archive node where they are made available for analysis (and distributed to redundant archives).

The `kotekan` pipeline is completely modular, composed of a string of unit tasks that perform some operation on the data. Some examples of pipeline tasks are to collect the streams from the array of GPU nodes, accumulate high cadence data streams down to lower rates, perform real-time calibration, or select subsets of data products to save separately. The pipeline can branch and produce multiple datasets in parallel. For the initial CHIME data acquisition period, the ultimate compression scheme was not ready to be implemented but it is infeasible to write out the full data rate to disk (referred to as N^2), so the pipeline was configured to select a subset of products and frequencies with higher sensitivity to save in the meantime. But having access to N^2 data is very valuable at this stage of the experiment for the purpose of characterizing the instrument, and the modularity of the pipeline allows saving a second data product composed of N^2 visibilities for only a handful of frequencies.

I have been heavily involved in the development of the receiver pipeline for the period following first light and leading up to the initial data acquisition run. In particular, I implemented a number of `kotekan` tasks required for the first run and overhauled the existing pre-archiver compression program to meet the performance requirements of the full CHIME data rate. I also helped with software deployment on the receiver system.

3 Noise integration in Pathfinder sky maps

The CHIME Pathfinder is a smaller scale telescope with the same design as CHIME, also located at the Dominion Radio Astrophysical Observatory in Penticton, BC. It has been operating as a test bed for CHIME systems and analysis since 2015. As of the fall of 2016, initial data acquisition

and calibration efforts had progressed sufficiently to generate stable sky maps on a daily basis. This project aimed to test the noise properties of these maps from day to day.

The dataset that was considered spanned 16 sidereal days, with some interruptions. Each day corresponds to a full scan of the visible sky from the latitude at Penticton, so the signal for every one is nominally identical. The visibility timestreams generated by the telescope measure the sky drifting through the beam as the Earth rotates. The time axis of the data therefore maps to an axis over right ascension (RA). Along the declination direction, the individual visibilities have a resolution that corresponds to the broad primary beam, covering an area of sky spanning from horizon to horizon. The structure along this direction can be resolved interferometrically by decoding the additional information stored in the array of visibilities. This is done by summing the visibilities weighted by the set of phases that exactly compensate for the delay between the signal received by each feed in the pair from a given declination. The signal from that direction adds constructively whereas the other directions on average cancel out. In this way, the visibility timestreams can be phased up to be sensitive to the sky at a specific declination, mapping out a ring on the celestial sphere. Doing this for a number of declinations produces a corresponding number of these rings that can be stitched together to form a 'ringmap'. These are formed on grids of pixels along the RA and declination directions, for every sidereal day. CHIME Pathfinder observes in the same band as CHIME, with 1024 frequency bins, but for this analysis only four pairs of adjacent frequencies were considered, chosen to span the full band and avoid its RFI contaminated regions. The pairs are located around (769.5, 644.1, 518.8, 443.8) MHz.

The goal of this project was to average a successively larger number of daily maps together and try and estimate the instrumental noise persisting in this integrated map at every step. If the instrumental noise in the maps is randomly distributed and uncorrelated from day to day, we expect from the central limit theorem that the RMS of this noise should drop off as the inverse of the square root of the number of daily maps that went into the average.

To estimate the noise level in a given map, the following procedure was used:

1. Select a patch of sky that excludes any bright sources and shows no visual anomalies, i.e. that appears to be mostly background.

2. Take a difference of the pairs of adjacent frequency bins to attempt to strip out the sky signal and leave only noise.

3. Form all possible subsets of days and take an average of the maps in each.

4. Compute the pixel-by-pixel RMS across all average maps of n days (of which there would be $\binom{N}{n}$ if there are N days in total).

5. Record the average of the pixel-by-pixel RMS across the entire map/patch as the estimated noise level for n days.

The results of the procedure outlined above are shown in Figure 11. The dashed line shows the expected $1/\sqrt{n}$ dependence, and the RMS results for increasing numbers of days are normalized to

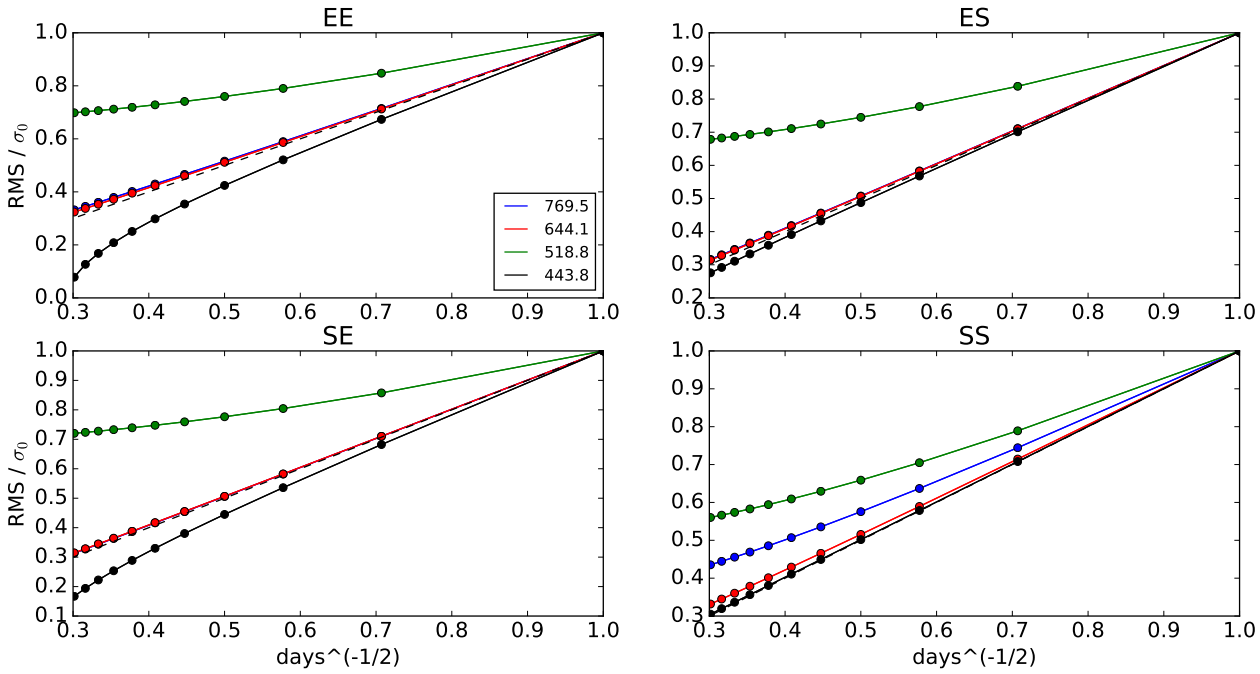

Figure 11: Estimate of noise level in an average of up to 16 Pathfinder ringmaps. The RMS is computed across pixels from a patch of sky that was chosen to be free of artifacts, after differencing adjacent frequency bins to remove sky signal. The colors indicate difference frequencies, given in the legend in MHz.

the average of the RMS accross individual days ($n = 1$). Two of the curves are close to the ideal case in all panels, indicating that at those frequencies the map patches were dominated by random noise. The green curve (518.8 MHz) does not average down nearly as quickly. Closer inspection of the maps at that frequency revealed that artifacts attributed to cross-talk between inputs were still present after processing. These features are correlated from day to day and make a plausible explanation for the high residual noise. More surprising is the black curve (443.8 MHz), which appears to be suppressed faster than $1/\sqrt{n}$. One way to obtain such behaviour would be for at least some days in the set to have features that are anti-correlated between them. Even if this affected only a few days from the set, it could be enough to alter the curve significantly, and would have a larger effect on its left side, where they would be present in a greater number of the combinations of days that are considered. Investigating the maps that were part of the set, such a feature was in fact found in a pair of days. This was hypothesized to be leftover sky signal from the frequency differencing. It happened that the difference ended up negative in one case and positive in the other, so that individually these maps increase the noise in the average, but if they are both present it is suppressed.

4 Telescope assembly

A significant portion of the work for this master's was spent assembling various components of the telescope over the course of regular visits to the construction site. These contributions to the experiment may also be among the most important, since they were direct and necessary steps towards the physical realisation of the instrument, a prerequisite to any subsequent analysis efforts. I will describe a few of these tasks to give a taste for this aspect of the project, starting with the assembly of the analog signal chain.

Feeds and focal line electronics The antennae are located along the focal lines of the cylindrical reflectors, numbering 256 per cylinder. They are attached to aluminum "cassettes" – boxes suspended on rails below the focal line walkway – which house the first stage amplifiers. Each of the cassettes holds fours feeds and eight amplifiers with trailing cables that join up in a connector plate. Every cassette (there are 256) was first assembled inside before being transported to the telescope focal line. The procedure for installing a cassette involved two people standing on the walkway who would attach ropes to its corners and swing the assembled cassette below the focal line and onto the rails. One would then lay flat on the walkway to adjust the cassette's position before securing it to the edge of the adjacent ones.

Each of the amplifiers then needed to be connected to the appropriate 50 m coaxial cable that carries the signal down to the receiver huts. To record all of these connections and ensure they were made in the right order, each component has a barcode serial number that would be scanned as they were connected.

Cable pulling The 50 m coaxial cables are routed from the receiver huts to the focal line through ducts that run up along walkway support legs (these are made from the same stuff as ventilation ducts). There are four ducts per cylinder, each holding 64 cables. These were pulled up in bundles of eight, using a specially designed spool that can unwind eight cables simultaneously. The procedure involved two people – one would be on the walkway hauling the cables while the other stayed at the bottom pulling them off the spool and shoving them into the duct. These cables are stiff and heavy so considerable force was required. However, care had to be taken to unwind them smoothly without introducing any kinks or torsion that would impact the performance of the coaxial transmission line. The bundles would initially be guided up the duct using a rope that would stay within the ducts throughout the process. Squeezing in the bundles without losing the rope could occasionally be challenging. Once the cables were in, they still needed to be arranged in trays that would support the extra lengths of cables with shorter spans on the focal line and connected to the bulkhead that allows the signals into the receiver huts, recording these connections along the way.

Layout database All of the connections between components of the telescope at a given time are recorded in a `MySQL` database. This centralized database is a very valuable tool for keeping track of the state of a complex instrument like CHIME and greatly facilitates the interpretation of the

data it produces. To ensure the accuracy and completeness of the layout database, it had to be populated as the components were installed, by recording the barcode serial numbers as mentioned above. This process was implemented in `Python` scripts running on a portable tablet computer that would guide the user through the installation process for a specific subsystem and save a record of the connections created. The connection data would then be automatically copied to a location accessible from UBC and added to the layout database. I helped to keep this system running and add new features as they became necessary, and was responsible for updating the database with the new connections.

Machining parts on the water-jet cutter A number of small mechanical parts that went into the CHIME assembly were made from bent aluminum sheet metal. For example, Figure 12 shows a part that supports the amplifiers in the cassettes and provides strain relief to the output cables – nicknamed the caribou due to its shape. The water-jet cutter was the ideal tool for prototyping these parts and producing them in the relatively small numbers needed for CHIME. I operated the machine and made hundreds of 'caribou' and a few other components for CHIME.

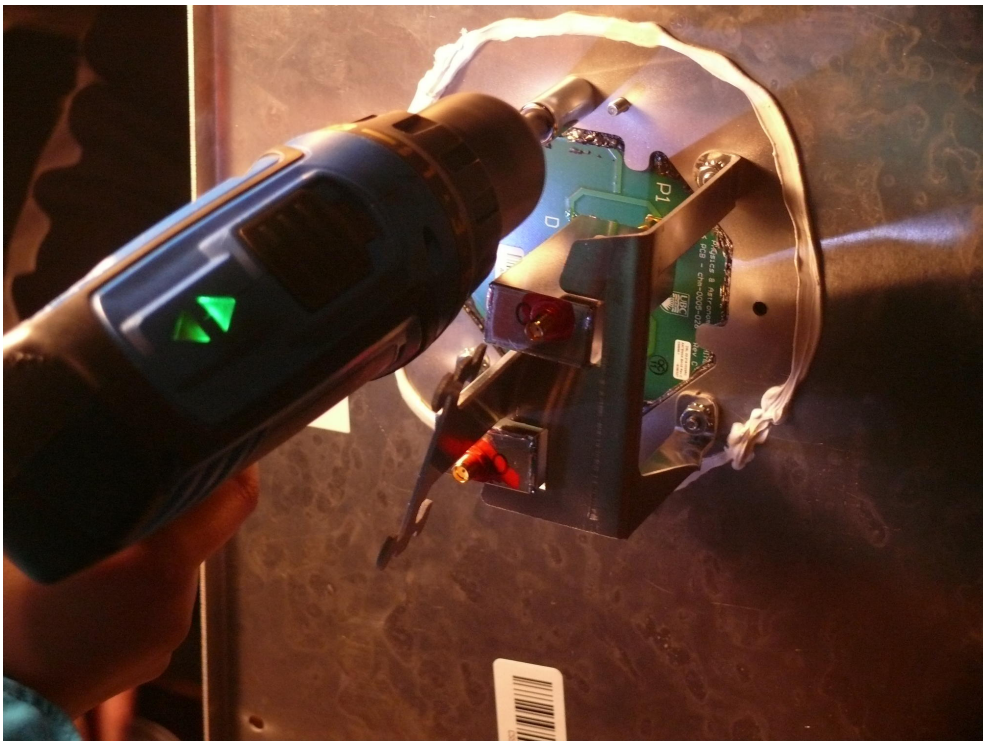

Figure 12: A CHIME feed with amplifiers being installed in a cassette, showing the 'caribou' support. (Photo taken by Mark Halpern.)

Focal line weatherproofing The first stage amplifiers, antenna feeds, and multiple cable connections are located on the focal line of the reflectors, beneath the walkway. Although the electronic components are housed in sealed enclosures and the walkways provide some shelter from the brunt

of the elements, more stringent weatherproofing will improve the stability and lifetime of the instrument. For instance, water accumulating near the feeds could change their dielectric properties, and regular exposure to the damp can promote corrosion. In addition, an unanticipated concern is to keep wildlife, birds specifically, from nesting near the electronics. It was realised during the operation of the Pathfinder that these small enclosed spaces, kept warm by the powered amplifiers, make desirable shelter for starlings. Sealing up in total nearly 400 m of elevated walkway is not a small task. I helped with installing flashing, caulk, chicken wire, weather stripping, etc. over a number of visits to site.

Receiver hardware Apart from my work on the FLA installation, I also participated in putting together other subsystems of the receiver and correlator. These tasks usually involved elaborate cable management. For instance, the 'X'-engine and 'F'-engine of the correlator are located in different RF-shielded huts, roughly 100 m apart, and the signals are transmitted between them over fibre optics. There is one dedicated fibre link for every frequency bin output by the channelizer, providing data to every one of the 1024 GPUs. There are thus 1024 fibres running between the huts. I helped with routing them on the GPU side, bringing the cables to the correct racks where the GPU nodes are mounted.

Conclusion

The past two decades have seen experimental cosmology develop at a rapid pace, with increasingly precise observations converging with remarkable consistency towards a rather simple model for the universe on the largest scales. However, significant questions remain unanswered – it appears the 'dark sector' is the dominant constituent of the universe – and tensions in the model parameters may be beginning to appear. Most notably, measurements of H_0 from the CMB and those from direct observation of recession velocities have developed a disagreement at the 3.7σ level. These questions call for further observations – especially in areas that have so far gone unexplored – that will provide either evidence for new physics or validation of the currently accepted theories. CHIME is poised to help shed light on at least two of these problems by measuring the BAO in a large volume at intermediate redshifts.

In this work, I have obtained sensitivity forecasts for the CHIME survey and propagated the results to produce expected constraints on the Hubble constant H_0 and dark energy equation of state parameter w. Independently of the CMB, CHIME together with measurements of the baryon density from deuterium abundance can constrain H_0 at $\sim 0.5\%$ precision. This is comparable to the precision attained from the CMB and much tighter than the errors on the distance ladder measurements. CHIME thus has the potential to distinguish between these two measurements and inform the interpretation given to the existing tension. In the event that CHIME and CMB find consistent values for H_0, combining them produces a joint constraint that is a mild improvement over CHIME alone. Constraints on w in contrast are greatly improved by combining CHIME with CMB observations. CHIME and deuterium can only provide $\sim 7\%$ errors on w, but these are reduced to $\sim 3\%$ when the CMB priors are included.

After years of design and construction, CHIME is now entering its operational stage. In the months and years to come, the focus will shift to calibration efforts and the development of analysis programs for cosmology. Future work will involve the refinement of the analysis presented here. In particular, reconstruction of the power spectrum into the non-linear regime has the potential to recover considerable signal-to-noise, as starkly illustrated in Figure 5. More realistic sensitivity forecasts could also be obtained by masking parts of the frequency band based on measurements of the RFI environment at the telescope site, as well as integrating instrumental window functions informed by the ongoing calibration development. As the survey progresses, these analysis programs can be put to the test on preliminary data products.

Bibliography

[1] G. E. Addison, D. J. Watts, C. L. Bennett, M. Halpern, G. Hinshaw, and J. L. Weiland. Elucidating ΛCDM: Impact of Baryon Acoustic Oscillation Measurements on the Hubble Constant Discrepancy. ApJ, 853:119, Feb. 2018. doi:10.3847/1538-4357/aaa1ed. → pages 5, 21

[2] S. Alam, F. D. Albareti, C. Allende Prieto, F. Anders, S. F. Anderson, T. Anderton, B. H. Andrews, E. Armengaud, É. Aubourg, S. Bailey, and et al. The Eleventh and Twelfth Data Releases of the Sloan Digital Sky Survey: Final Data from SDSS-III. ApJS, 219:12, July 2015. doi:10.1088/0067-0049/219/1/12. → page 5

[3] É. Aubourg, S. Bailey, J. E. Bautista, F. Beutler, V. Bhardwaj, D. Bizyaev, M. Blanton, M. Blomqvist, A. S. Bolton, J. Bovy, H. Brewington, J. Brinkmann, J. R. Brownstein, A. Burden, N. G. Busca, W. Carithers, C.-H. Chuang, J. Comparat, R. A. C. Croft, A. J. Cuesta, K. S. Dawson, T. Delubac, D. J. Eisenstein, A. Font-Ribera, J. Ge, J.-M. Le Goff, S. G. A. Gontcho, J. R. Gott, J. E. Gunn, H. Guo, J. Guy, J.-C. Hamilton, S. Ho, K. Honscheid, C. Howlett, D. Kirkby, F. S. Kitaura, J.-P. Kneib, K.-G. Lee, D. Long, R. H. Lupton, M. V. Magaña, V. Malanushenko, E. Malanushenko, M. Manera, C. Maraston, D. Margala, C. K. McBride, J. Miralda-Escudé, A. D. Myers, R. C. Nichol, P. Noterdaeme, S. E. Nuza, M. D. Olmstead, D. Oravetz, I. Pâris, N. Padmanabhan, N. Palanque-Delabrouille, K. Pan, M. Pellejero-Ibanez, W. J. Percival, P. Petitjean, M. M. Pieri, F. Prada, B. Reid, J. Rich, N. A. Roe, A. J. Ross, N. P. Ross, G. Rossi, J. A. Rubiño-Martín, A. G. Sánchez, L. Samushia, R. T. Génova-Santos, C. G. Scóccola, D. J. Schlegel, D. P. Schneider, H.-J. Seo, E. Sheldon, A. Simmons, R. A. Skibba, A. Slosar, M. A. Strauss, D. Thomas, J. L. Tinker, R. Tojeiro, J. A. Vazquez, M. Viel, D. A. Wake, B. A. Weaver, D. H. Weinberg, W. M. Wood-Vasey, C. Yèche, I. Zehavi, G.-B. Zhao, and BOSS Collaboration. Cosmological implications of baryon acoustic oscillation measurements. Phys. Rev. D, 92(12):123516, Dec. 2015. doi:10.1103/PhysRevD.92.123516. → page 21

[4] R. J. Cooke, M. Pettini, and C. C. Steidel. One Percent Determination of the Primordial Deuterium Abundance. ApJ, 855:102, Mar. 2018. doi:10.3847/1538-4357/aaab53. → pages 21, 22, 24

[5] S. Dodelson. *Modern cosmology*. Academic Press, San Diego, CA, 2003. URL https://cds.cern.ch/record/1282338. → pages 7, 18

[6] D. J. Eisenstein, H.-J. Seo, and M. White. On the Robustness of the Acoustic Scale in the Low-Redshift Clustering of Matter. ApJ, 664:660–674, Aug. 2007. doi:10.1086/518755. → pages 12, 19

[7] G. Hinshaw, D. Larson, E. Komatsu, D. N. Spergel, C. L. Bennett, J. Dunkley, M. R. Nolta, M. Halpern, R. S. Hill, N. Odegard, L. Page, K. M. Smith, J. L. Weiland, B. Gold, N. Jarosik,

A. Kogut, M. Limon, S. S. Meyer, G. S. Tucker, E. Wollack, and E. L. Wright. Nine-year Wilkinson Microwave Anisotropy Probe (WMAP) Observations: Cosmological Parameter Results. ApJS, 208:19, Oct. 2013. doi:10.1088/0067-0049/208/2/19. → page 5

[8] E. Hubble. A relation between distance and radial velocity among extra-galactic nebulae. *Proceedings of the National Academy of Sciences*, 15(3):168–173, 1929. ISSN 0027-8424. doi:10.1073/pnas.15.3.168. URL http://www.pnas.org/content/15/3/168. → page 4

[9] N. Kaiser. Clustering in real space and in redshift space. MNRAS, 227:1–21, July 1987. doi:10.1093/mnras/227.1.1. → page 18

[10] A. Lewis and S. Bridle. Cosmological parameters from CMB and other data: A Monte Carlo approach. *Phys. Rev.*, D66:103511, 2002. doi:10.1103/PhysRevD.66.103511. → pages ix, 13, 14, 21

[11] K. W. Masui, E. R. Switzer, N. Banavar, K. Bandura, C. Blake, L.-M. Calin, T.-C. Chang, X. Chen, Y.-C. Li, Y.-W. Liao, A. Natarajan, U.-L. Pen, J. B. Peterson, J. R. Shaw, and T. C. Voytek. Measurement of 21 cm Brightness Fluctuations at z ˜ 0.8 in Cross-correlation. ApJ, 763:L20, Jan. 2013. doi:10.1088/2041-8205/763/1/L20. → page 2

[12] K. A. Olive, G. Steigman, and T. P. Walker. Primordial nucleosynthesis: theory and observations. Phys. Rep., 333:389–407, Aug. 2000. doi:10.1016/S0370-1573(00)00031-4. → page 21

[13] Planck Collaboration, P. A. R. Ade, N. Aghanim, M. Arnaud, M. Ashdown, J. Aumont, C. Baccigalupi, A. J. Banday, R. B. Barreiro, J. G. Bartlett, and et al. Planck 2015 results. XIII. Cosmological parameters. A&A, 594:A13, Sept. 2016. doi:10.1051/0004-6361/201525830. → pages 5, 19, 22, 23, 24

[14] A. G. Riess, S. Casertano, W. Yuan, L. Macri, J. Anderson, J. W. MacKenty, J. B. Bowers, K. I. Clubb, A. V. Filippenko, D. O. Jones, and B. E. Tucker. New Parallaxes of Galactic Cepheids from Spatially Scanning the Hubble Space Telescope: Implications for the Hubble Constant. ApJ, 855:136, Mar. 2018. doi:10.3847/1538-4357/aaadb7. → page 5

[15] H.-J. Seo and D. J. Eisenstein. Probing dark energy with baryonic acoustic oscillations from future large galaxy redshift surveys. *Astrophys. J.*, 598:720–740, 2003. doi:10.1086/379122. → page 15

[16] H.-J. Seo and C. M. Hirata. The foreground wedge and 21-cm bao surveys. *Monthly Notices of the Royal Astronomical Society*, 456(3):3142–3156, 2016. → page 18

[17] H.-J. Seo, E. R. Siegel, D. J. Eisenstein, and M. White. Nonlinear structure formation and the acoustic scale. *The Astrophysical Journal*, 686(1):13, 2008. URL http://stacks.iop.org/0004-637X/686/i=1/a=13. → page 15

[18] J. R. Shaw. Cora. https://github.com/radiocosmology/cora, 2017. → page 19

[19] J. R. Shaw, K. Sigurdson, M. Sitwell, A. Stebbins, and U.-L. Pen. Coaxing cosmic 21 cm fluctuations from the polarized sky using m -mode analysis. Phys. Rev. D, 91(8):083514, Apr. 2015. doi:10.1103/PhysRevD.91.083514. → pages 12, 15

[20] J. Silk. Cosmic Black-Body Radiation and Galaxy Formation. ApJ, 151:459, Feb. 1968. doi:10.1086/149449. → page 15

[21] S. Weinberg. *Cosmology*. Oxford University Press, Oxford, NY, 2008. → page 7